Github repo: Cisneros-Galaxy/RCFM

Usage: Secondary publications and information retrieval purposes.

PACS numbers: May be entered using the `\pacs{#1}` command.

DRAFT- Rotation Curve Fitting Model

Sophia Natalia Cisneros
Department of Astronomy, University of Washington

Richard Ott*
Affiliate

Meagan Crowley†
Colorado School of Mines

Amy Roberts‡
CU Denver

Marcus Paz, Zaneeyiah Brown, Landon Joyal, Roberto Real Rico, Elizabeth Gutierrez-Gutierrez, Phong Pham, Zac Holland, Amanda Livingston, Lily Castrellon, Summer Graham, Shanon J. Rubin, Aaron Ashley, Dillon Battaglia, Daniel Lopez, and Maya Salwa

(Dated: September 30, 2023)

One key piece of evidence for dark matter is the flat rotation curve problem: the disagreement between measured galactic rotation curves and their luminous mass. A novel solution to this problem is presented here. A model of relativistic frame effects on Doppler shifts due to the slightly curved frames of an emitting galaxy and the Milky Way is derived. This model predicts observed Doppler shifted spectra (in excess of the luminous mass) based only on the observed luminous matter profile and one free model parameter. It fits well 172 of the 175 galaxies reported in the SPARC database of galactic rotation profiles and photometry measurements. The resulting fits have an average $\chi^2_r = 4.14$, competitive with current MOND-RAR average $\chi^2_r = 4.22$ on the same sample of galaxies. We also make a few comparisons to dark matter fits to well known galaxies. Implications of this model in explaining other observed phenomena related to galactic curves are discussed.

I. INTRODUCTION

The flat-rotation curve problem is the divergence of two rotation velocities about the center of a spiral galaxy, which come from different observations of light [1–3]. The observations are photometry and Doppler shifted spectra. Photometry gives the expected, Keplerian orbital velocities which descend past the stars. Doppler shifted spectra gives the "flat-rotation curve" velocities, which remain essentially constant far past luminous matter. The divergence of these two velocities (Fig. 1) is primary evidence for dark matter theories.

Dark matter is hypothesized to be massive particles which are electromagnetically neutral, and have a very low interaction probability with baryonic matter. Though searches for direct detection continue, in the absence of a definitive understanding of dark matter particles [4], the paradoxes of dark matter theories remain interesting. S. McGaugh notes one such paradox when he asks "Why is the luminous tail wagging the dark matter dog, if dark matter dominates dynamics ?" [5, 6]. This references the curious fact that knowledge of the stellar disk completely determines the spherical dark matter halo[7].

Another interesting paradox is found in the Universal Rotation Curve (URC), which is a spectrum of 1,100 rotation curves (RCs), each galaxy normalized by its scale-length [8–11]. Strangely, in this spectrum of RCs, galaxies' RC are separated by size. Those galaxies larger than the Milky Way have RCs which inflect down towards truly "flat" RCs, and those smaller than the Milky Way have RCs which inflect up towards flat. The presumed RC of the Milky Way's (MW) sits in the middle. We will interpret this as evidence of frame dependent effects in our observations of Doppler shifted spectra. In dark matter theories this curious phenomenology requires fine-tuning which reduces the predictivity of dark matter models [12]. This phenomenology is accounted for in dark matter theories with the phrasing that small galaxies require "maximal dark matter halos", and those larger than the Milky Way require only "minimal dark matter halos". In fact, though dark matter theory is built from the tenets of classical gravity, this interpretation contradicts standard gravity. In classical gravitation theory, mass accretion rates are directly proportional to the initial mass function [13]. Interpreting this paradox in a framework of frame dependency due to the Milky Way relieves this conflict, and replaces dark matter with relative gravitational frame effects.

To construct a paradigm of relative frame effects, we look at Modified Newtonian Dynamics (MOND) [15], the leading alternative to dark matter in this context. MOND is successful at fitting a large distribution of galaxy RC without dark matter particles, but modifies standard gravitational physics on the length scales of galaxies. In the MONDian paradigm the luminous mass is the only mass, but excesses in Doppler shifted spectra are still interpreted as physical rotation velocities. The velocities in excess of the Keplerian expectations from luminous mass are explained by a chang-

* rich.ott@EMAIL.com
†
‡ CU

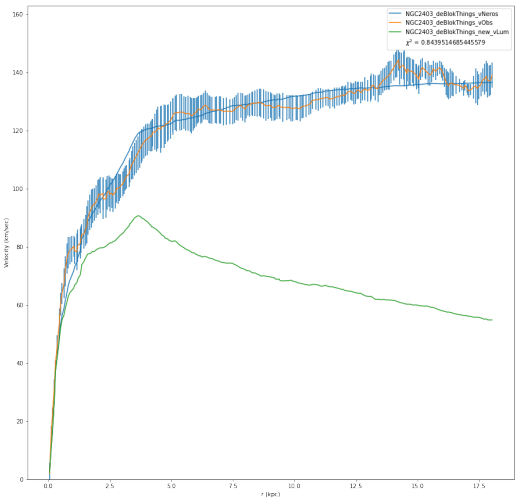

FIG. 1: NGC 2403 rotation curve data (orange line) and baryon model (green line) from de Blok *et al.* [14]), fitted by the RCFM (blue line) presented in this paper

ing acceleration due to gravity [16]. MOND's free parameter is essentially constant, representing the changing acceleration scale [17], but distance is also a free parameter which is in conflict with distances inferred from standard candles for some notable galaxies. In this new frame-dependent picture, we attribute the MONDian successes with a changing acceleration scale to a effective characterization of the role of the Milky Way on our observations, but show that our new RC fitting formula is more adaptive and fits a wider range of galaxies, with fewer free parameters and at reported distances, with no modification of current gravitational physics. So, while MOND remains a fundamental alteration to gravity, our proposed theory reinterprets MOND as a relativistic effect that can be extended with a mapping technique from Einstein's gravitational physics. Previous attempts to extend MOND to the relativistic regime have given rise to new theories of gravity [18–20]. The heuristic technique we propose here, reproduces the fitting successes of MOND while improving on notable problem galaxies but does not modify physics.

Previous consideration of relative gravitational effects in the flat-rotation curve problem used Galilean differences between redshifts at the large r limit of the observations instead of the Lorentz-type maps we will invoke here [21]. The form of the Lorentz Doppler shift formula which leads to the dark matter problem in spiral galaxies is applicable for the relative motion of inertial frames in a flat spacetime. The new rotation curve fitting model (RCFM) is constructed in **Section II**, and in **Section III** we fit a sample of 175 well known galaxies (SPARC [17]) in comparison to MOND and dark matter theories fits to the same galaxy data. In **Section IV** we discuss RCFM results in comparison to dark matter, MOND- RAR (Radial Acceleration Relation) [6, 16, 17, 22] models, and show that there exists a tight correlation between our free parameter and a ratio of two photometric observations (luminosity and half light radius of the galaxy). In **Section V** we conclude with a discussion of upcoming observations which can further constrain this model.

II. ROTATION CURVE FITTING MODELS

A. Dark matter rotation curve fitting formula

The dark matter rotation curve (RC) formula is

$$v(r)^2_{rot} = v(r)^2_{lum} + v(r)^2_{dm}, \tag{1}$$

where terms in $v(r)_{lum}$ are the Keplerian velocities from estimates of luminous mass, $v(r)_{dm}$ are the velocities attributed to dark matter, and terms in $v(r)_{rot}$ are the model prediction. In theory, terms in $v(r)_{rot}$ are fitted to terms $v(r)^2_{obs}$ from Doppler shifted spectra. All velocities are assumed those of test particles in circular orbits, in the plane of the stellar disk, about the rotation axis of the galaxy at $r = 0$.

In practice, the functional form of dark matter and $v(r)^2_{dm}$ comes from the algebraic difference of the quadratic terms $v(r)^2_{obs}$ (Doppler shifts) and $v(r)^2_{lum}$ (Luminous mass), which explains why the luminous tail is wagging the dark matter dog [5, 6], because our formulation of dark matter comes from observations of the luminous mass.

B. Two observations of light

The observables in the flat-rotation curve problem are the Doppler shifted spectra and photometry. Doppler shifted spectra give RC velocities $v_{obs}(r)$ by a flat spacetime Lorentz boost

$$\frac{v_{obs}(r)}{c} = \frac{\left(\frac{\omega'(r)}{\omega_o}\right)^2 - \left(\frac{\omega_o}{\omega'(r)}\right)^2}{\left(\frac{\omega'(r)}{\omega_o}\right)^2 + \left(\frac{\omega_o}{\omega'(r)}\right)^2}, \tag{2}$$

for ω_o the characteristic lab frequency and $\omega'(r)$ the observed shifted frequency. The vacuum light speed is c.

Photometry gives a measure of total light, which is then associated with mass by a mass-to-light ratio from a population synthesis models (PSM). PSM rely upon a complex suite of assumptions regarding galaxy evolution, metallicities and initial mass functions [23, 24], and are under-constrained [25, 26] due to the dark matter problem, producing an error budget of $\approx 20\%$ [17]. That said, while one galaxy may have a diverse collection of possible luminous mass models, all such models descend in a Keplerian fashion outside of the stars.

Mass models give estimates of the Newtonian gravitational potential by

$$\Phi(r) = -\int_{r_{ref}}^{r} \vec{g} \cdot \vec{dr}. \tag{3}$$

for r the field point, and r_{ref} the reference point, and g the acceleration due to some gravitational field. The classical boundary condition is that the potential go to zero at $r' = \infty$. This potential solves the Poisson equation

$$\nabla^2 \Phi(r)_{lum} = 4\pi G \rho(r'). \tag{4}$$

For $\rho(r')$ the mass density distribution, and G is Newton's constant. The gradient in the potential gives the circular orbital velocities v_{lum} (Eq. 1) by the central force relation

$$\frac{\partial\Phi(r)_{lum}}{\partial r} = \frac{v(r)^2_{lum}}{r}, \tag{5}$$

which is the origin of the quadratic sum in the dark matter RC formula (Eq. 1). The baryonic components are reported as stellar disk, stellar bulge, and a gas halo

$$v(r)^2_{lum} = \gamma_b v(r)^2_{bulge} + \gamma_d v(r)^2_{disk} + v(r)^2_{gas}. \tag{6}$$

Gas fractions v_{gas}, however, are calculated from different observational technique as given in [27], and do not require mass-to-light ratios. By use of the quadratic sums, it is clear that what we're characterizing in the flat-rotation curve problem is a sum of gradients, and which will motivate our replacement of the dark matter term with a galaxy mapping onto the Milky Way.

C. New rotation curve fitting model (RCFM)

The physical paradigm for the new rotation curve fitting model (RCFM) is that the luminous mass is the only mass and the velocity $v(r)_{lum}$ is the only velocity (due to the luminous mass interpreted by Poisson dynamics). We propose that excesses in Doppler shifted spectra, usually encapsulated in the dark matter contribution v^2_{dm} (Eq. 1) be directly replaced with a product of two Lorentz-type maps S_1 and S_2 representing the frame-dependent effects due to the Milky Way and galaxy frames,

$$v(r)^2_{rc} = v(r)^2_{lum} + \alpha\kappa(r)^2 S(r)_1 S(r)_2. \tag{7}$$

By following this prescription we implicitly assume that contributions to Doppler shifted spectra from relative frame motion (v_{lum}, Eq. 6) and those from relative curvature ($S_1 S_2$) are roughly separable as in Eq. 7 [28, 29]. For clarity in what follows, we now drop explicit functional dependence on r. All terms can be assumed to be evaluated one-to-one in radius between the galaxy being observed and the Milky Way, with the exception of the model's free parameter α, which is single valued for each galaxy fitted. Constants like Newton's G and the speed of light c will be set to 1.

D. RCFM heuristic derivation

The RCFM galaxy maps onto the Milky Way (S_1 and S_2 in Eq. 7) are constructed from the tetrad formalism of general relativity [30], in which we make use of the fact that inertial frame fields can be attached to any point on a curved manifold so that locally, the physics of general relativity is indistinguishable from that of special relativity [31]. These frame fields e^μ_a are related to the curved spacetime metric $g^{\mu\nu}$ in the following way

$$g^{\mu\nu} = e^\mu_a e^\nu_b \eta^{ab} \tag{8}$$

for η^{ab} the local flat spacetime Minkowski metric. In the frame field formalism "when going from one local inertial frame at a given point to another at the same point, the fields transform with respect to a Lorentz transformation"[32]. Our goal then, is to use Lorentz-type functions to map galaxies one-to-one in radius onto the Milky Way, using the weak field Schwarzschild time coefficients $g_{00} = -(1 - 2\Phi)$, as the weak-field timelike Schwarzschild field frames are defined by

$$e^0_0 = \sqrt{1 - 2\Phi}. \tag{9}$$

Terms in Φ are the Newtonian gravitational potential[33]. Classically, the Φ of galaxies are integrated from a value of $\Phi = 0$ at the large limit $r \to \infty$, into a negative maxima at the small r limit (Eq. 3). This is an implicit assumption of a globally flat embedding space, which ensures that the potential goes to zero at a distance of infinity from the mass distribution.

However, recent observations [34, 35] have shown that on the relevant length scales of galaxies and groups of galaxies we have not recovered flat spacetimes. In fact, the external environments of galaxies and flowlines of groups of galaxies are exceedingly complex and diffusely populated with matter, demonstrating structure with sources and sinks. In addition, the value of the vacuum energy remains an outstanding physics problem [36]. In the absence of definite knowledge of the values of Φ at the large r limit of individual galaxies, and since all RCFM terms are ratios of terms in g_{00} for two galaxies, we instead inform the integration of the gravitational potentials from Wolfgang Rindler's statement that "the center of each galaxy provides a basic local standard of nonacceleration ... so then can be treated like a local inertial frame relative to its own center"[37].

From Rindler's insight, to compare galaxies as inertial frames is to compare them from their centers, so we integrate galaxy potential from a value of zero at the $r \approx 0$, out to the large R limit of the data. Computationally, this produces positive definite gravitational potentials, summed from $\Phi = 0$ at $r \approx 0$ and increasing to a constant value. These potentials are then subtracted from 1 in the clock term $g_{00} = -(1 - 2\Phi)$. Gravitational potentials calculated in this way still obey Poisson's equation Eq. 4 and the central force law Eq. 5.

Using this process to calculate the Φ terms, we find that best fit functions for S_1 is

$$S_1 = \sinh\zeta, \tag{10}$$

with a rapidity defined by the gravitational field frames

$$e^\zeta = \sqrt{\frac{g_{00}|_{gal}}{g_{00}|_{mw}}}, \tag{11}$$

for $g_{00}|_{gal}$ assigned to the galaxy sending the signals, and $g_{00}|_{mw}$ for the Milky Way, evaluated one-to-one in radius.

The second transformation is

$$S_2 = \cosh\tau \tag{12}$$

for the rapidity angle τ defined by the Lorentz exponential term

$$e^\tau = e^{(\zeta+\eta)/2}. \tag{13}$$

where e^τ is a convolution of the curved 2-frame exponential e^ζ (Eq. 11) with the flat 2-frame exponential e^η

$$e^\eta = \sqrt{\frac{1+\beta}{1-\beta}}. \tag{14}$$

for $\beta = v_{lum}/c$ the Keplerian velocities expected from estimates of the luminous mass. This last step is necessary is due to the fact that observations are made in locally flat frames, as evidenced by the constancy of the speed of light. In the flat 2-frame the metric is Minkowski $\eta^{\alpha\beta}$. Use of Eq. 14 is a statement that Keplerian RCs are a good estimate of flatness, since dark matter is not required to reproduce the RC of our Solar System, or possibly our Milky Way [38].

In Eq. 7, α is the RCFM free fitting parameter, which has a different value for each galaxy fitted, and κ is a measure of relative curvature

$$\kappa = \frac{\Phi_{gal}}{\Phi_{mw}}. \tag{15}$$

Previously, Rindler extended the transforms of special relativity to accelerated frames on a flat background [39]. Viewed as Rindler's accelerated coordinates, S_1 is timelike and S_2 is spacelike [21, 33, 37]. We have previously explored the space of hyperbolic transformations in [40–43], and find the above to be the best fit functions.

E. Geometric simplifications

Population synthesis models commonly assume spherical symmetry for the stellar bulge, gas halo, but axial symmetry for the stellar disk [44, 45]. However, it is a common calculational tool to use spherical symmetry for the entire integrated potential of the luminous mass distribution [18, 46], because numerical integration of the thin disk is computationally intensive, requiring assumptions of underconstrained boundary conditions and relevant physical scales, which therefore add extra free parameters to the problem [47]. We use the Schwarzschild metric as the simplest spherically symmetric representation to capture the relevant physics of the problem, without excess computations. A more detailed analysis might use the interior Schwarzschild metric as well as the full disk potential. We have previously tested the Kerr Doppler shift in this context [29], but have found the difference from Schwarzschild predictions are below the observational limits.

Gravitational potentials calculated for the same mass distribution in a spherically symmetric geometry converge to those calculated for an exponential disk at lengths greater than one-third of the exponential scale-length of the disk R_e, ie. $r > R_e/3$ [48], the region where dark matter effects becomes important [3]. However, in the inner regions the spherical assumption overestimates the potential of a thin disk by a factor of ≈ 2 in the region between the center and $R_e/3$. Since the RCFM fits compare galaxy structure from the centers, the impact of the spherical assumption can be seen in high mass-to-light ratios for some galaxies, though on average are not statistically higher than MOND or dark mattermodels.

III. DATA

A. SPARC Galaxies

We fit the Spitzer Photometry and Accurate Rotation Curves (SPARC) dataset of 175 nearby galaxies with extended RC data from atomic hydrogen (HI) and H-α [17]. HI provides the most reliable RCs because it is dynamically cold, traces circular orbits, and can be observed several effective radii past the stellar disk. This sample of rotationally supported galaxies spans the widest range of masses and morphologies presently available.

These galaxies are accompanied by photometry, represented by Keplerian model RCs for each galaxy, from the Spitzer Photometry in the near infrared at $3.6\mu m$. Near infrared is currently believed to be the best tracer of stellar mass in population synthesis models (PSM) [24], as at this wavelength, mass-to-light (γ_i) ratios are almost constant independent of star formation history [23, 24]. The SPARC database reports mass-to-light ratios of $\gamma_i = 1$ in units of $M_\odot/L_\odot$ at $3.6\mu m$. Gas fractions v_{gas} are calculated from surface density profiles of HI with the formalism given in [27] and scaled a factor 1.33 to account for cosmological helium abundances. Contributions from molecular gas are ignored because CO data are not available for most SPARC galaxies. Error on these velocities is estimated at 20% [17]. The SPARC database can be found at `http://astroweb.cwru.edu/SPARC/`.

B. Milky Way

The RCFM requires a static choice for the baryon distribution of the Milky Way (MW). Mass-modeling of the MW is a famously under-constrained problem, due to our observing position from within the disk [49].

We test the RCFM using two different MW luminous mass models; a hybrid model combined from Xue *et al.* [50], Sofue [51], [52], and a model from McGaugh [53]. The Sofue and Xue MW are derived from the same data and same model constraints, but are combined for maximal coverage, with the Sofue model from $[0, 20]$ kpc (Sofue [51]) and the Xue model from $[20, 60]$ kpc (Xue *et al.* [50]).

The two Milky Way models vary in their underlying assumptions regarding structure and gravitational behavior of the Milky Way. For example, McGaugh [53] assumes a galactic bar at the center and thus does not include velocity data of the inner 5 kpc of the Milky Way. In contrast, the Xue-Sofue MW is centrally condensed, and the peak velocity is at around 94 parsecs, versus that of the McGaugh MW at approximately 6.55 Kpc [53]. See Table I for more information. In the current work, we do not see a strong signal to prefer either model. The MW gravitational potentials are calculated in the same way as described in Sec. II D.

IV. ANALYSIS AND RESULTS

A. fitting procedure

To fit galaxies in the SPARC sample, the fitting procedure is as follows. First, a Milky Way model is chosen (see Sec. III B) and the data read in as v_{lum} for a series of measurements in radii. The galactic potential is computed as described (see Sec. II D), by numerically integrating

$$\Phi(r) = \int_{inner}^{outer} dr \frac{v_{lum}^2}{r}. \tag{16}$$

Once the MW potential is calculated, it remains static for the rest of the fitting procedure.

The data for the galaxies being observed include several pieces of information: the RC velocities v_{obs} from Doppler

TABLE I: Comparison of the two Milky Way models used in this paper

Milky Way Model	Photometry	Model dependence	Rotation Curve data	scale radius bulge	γ_{bulge}
Xue-Sofue	$2.2\mu m$	NFW [54]	SDSS DR6 [50]	$Rb = 0.5$ kpc	$7.1 M_\odot/L_\odot$
McGaugh	$3.6\mu m$	MOND [15]	CO data [55]	N.A. bar assumed	N.A. bar

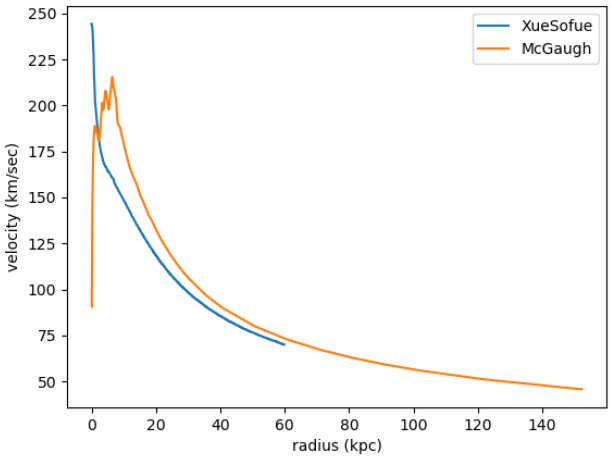

FIG. 2: Milky Way models used in this work [52], [53]

shifted spectra, the uncertainty on that measurement v_{err}, and the components of the luminous mass interpreted as orbital velocities, v_{bulge}, v_{disk}, and v_{gas}. To calculate the baryonic potential for the galaxy in question, v_{lum} is first computed as per Eq. 6, for $\gamma_b = 1$ and $\gamma_d = 1$. The Φ_{gal} associated with that galaxy is then computed as in Eq. 16.

After the Φ for the galaxy being studied and the Milky Way have been calculated, the components must be compared at matching values of r. To match radii, the Φ_{MW} are calculated at interpolated radii as reported in the RC data v_{obs} for the galaxy being observed. Any point with a radius larger than the largest radius in the Milky Way model is discarded.

The RCFM prediction is assembled as in Eq. 7, to give a predicted v_{rc} which is fitted to the RC data v_{obs}. The fit is then minimized to find the lowest χ^2, using the `scipy.optimize.curve_fit` utility in Python. The equations outlined in Section II contain free parameters that must be determined for each galaxy fit. The choice of the static Milky Way luminous mass profile is chosen before fitting. The model's free parameter α starts from an initial value of $\alpha = 0.01$, and mass-to-light parameters from an initial value of 1.00, and then all parameters are allowed to vary freely and to be determined by minimization of the χ^2. Reported gas fractions are fixed at their reported values (HI scaled for Helium abundance by a factor of 1.33 in the SPARC database), though addition of molecular gas could increase mass fractions in the inner kiloparsec of a galaxy [7]. There are three of 175 SPARC galaxies which do not converge to an RCFM solution; UGC06628, UGC04305 and F561-1. These are all irregular galaxies in the Hubble classification scheme, and the restriction on the gas fractions in our code may limit our ability to find solutions given the reported data.

B. Evaluating Goodness-of-fits

There are two metrics by which different model RC fits are judged, the reduced χ^2 values and the mass-to-light ratios from fits as compared to PSM. Reported error estimates on RC velocities have not been standardized across the field [56, 57], so χ^2 comparisons only have meaning when fitted to the same RC data. We compare χ^2 values for RCFM fits to the RC data in the SPARC database [17], previously fitted by the a MOND extension called the Radial-Acceleration-Relation (MOND-RAR)[6, 22, 58].

In MOND-RAR, the global acceleration relation is

$$g_{obs} = \frac{g_{bar}}{1 - e^{-(\sqrt{g_{bar}/g_\dagger})}} \tag{17}$$

for all terms in g_i the gradients of the potentials as in Eq. 5, that due to the baryons is g_{bar} with an assumed intrinsic error of 10% on the HI flux and 25% on the mass-to-light ratios, the RC data represented by g_{obs}, and the changing acceleration scale $g_\dagger = 1.20 \pm 0.02(\text{random}) \pm 0.24(\text{systematic}) \times 10^{-10}\text{m/s}^2$ [6]. MOND-RAR and RCFM fits are compared in Table IX and Table II, dark matter results are included when SPARC galaxies have previously been fitted. RCFM values are remarkably low, providing confidence in the faithfulness of the model to galaxy RC data.

In Table II the average mass-to-light ratios for the entire sample are given for both RCFM and MOND-RAR fits , in comparison to expectations from PSM McGaugh *et al.* [6]. We note that the spherical approximation we use for simplicity and computational reasons, as described in Sec. II E, results in mass-to-light ratios for the disk which are higher than PSM by approximately a factor of 2.

TABLE II: DINGDONG Average Results from MOND-RAR and RCFM fits to 172 SPARC galaxies

Model	γ_d	γ_b	χ^2_{red}
PSM [6]	0.5	0.7	—
MOND-RAR	0.64	0.73	4.27
RCFM-XueSofue	1.13	0.95	4.14

(a) The γ_i are in units of solar mass per solar luminosity $M_\odot/L_\odot$. Results are with respect to the McGaugh MW model.

C. Comparing Milky Way Models

The residuals of fits to the SPARC sample were used to compare different MW models (see Sec. III B). Histograms of residuals normalized by the error in velocity observations are shown in Fig. 3. In all cases, residuals of model fits to observed velocity data followed a narrow distribution centered at zero with a range of ± 3 km/s, albeit with heavy tail features. The behavior of the residuals did not vary greatly between MW models, suggesting that the fitting parameters in our model are robust with respect to differing Milky Way

model assumptions at this present level of analysis. With a finer grained analysis and a larger sample, the degeneracy between MW models could be resolved.

A Gaussian fit on residuals from fits using the McGaugh MW model gave a mean of -0.027 km/s, standard deviation of 0.841 km/s and a full-width half-maximum (FWHM) of 1.980 km/s, whereas a Gaussian fit to the residuals from fits using the Xue-Sofue MW model gave a mean of -0.012 km/s, standard deviation of 0.819 km/s and a FWHM of 1.928 km/s. The small values associated with these quantities in both cases provide confidence that our fits match data closely.

Yet, the Gaussian fits did not quite capture the full peak and heavy tails in the residuals. This suggests that there may be non-Gaussian error in the observations of galaxy velocities. To address this, the residuals were also fit to an exponential function shown in Fig. 3. The exponential function captured both the peak and the heavy-tailed behavior of the distributions more faithfully.

D. Model Comparisons for Individual Galaxies

In this section we will compare RCFM fits to MOND-RAR and dark matter models.

1. NGC 2841

NGC 2841 is a star dominated spiral galaxy, which historically has been regarded as a problematic case for MOND Gentile *et al.* [57]. MOND-RAR finds a good fit for this galaxy after adjusting the Cepheid distance of 14.1 Mpc, by 1σ, to 15.5 Mpc. The RCFM fit is accomplished at the Cepheid distance, and has a comparable reduced χ^2 to the MOND-RAR fit. The resulting γ_d are also commensurate. The RCFM fit is shown in Fig. 4.

2. IC 2574

IC 2574 is a gas dominated dwarf galaxy. Figure 5 shows the RCFM fit. MOND-RAR finds a good fit to this galaxy but adjusts the distance and inclination by 1 to 1.5σ, and their resulting disk mass-to-light $\gamma_d = 0.07$ is very low. This galaxy is problematic for dark matter model fits, as the dark matter model significantly overestimates the RC to 10 kpc, [59]. RCFM fit results for this galaxy successfully, at the reported tip of the red giant branch distance of 3.91 Mpc, give $\gamma_d = 0.553$.

3. NGC 3198

NGC 3198 has historically been a problem for MOND fits when the distance is a free parameter [57], as the preferred distance for MOND fits is 2σ smaller than that reported from the most reliable distance indicator, Cepheid variable stars. MOND-RAR fits reproduce this distance preference, using a distance of $D = 10.4 \pm 0.4$ Mpc [22]. With this fit, MOND-RAR gives a reduced $\chi^2 = 2.057$, and $\gamma_d = 0.77 \pm 0.03$. The RCFM fit to NGC 3198 at the Cepheid distance of 13.8 Mpc, yields a better reduced $\chi^2 = 1.676$, and mass-to-light ratios of $\gamma_d = 0.439$. See Fig. 6.

4. Comparison of NGC 7814 and NGC 891

The NGC 7814 and NGC 891 galaxies present an interesting conundrum for dark matter and MOND models. Both galaxies are presented edge-on on the sky, and both have essentially identical RCs, but are extreme opposites in morphologies. NGC 7814 is a bulge dominated galaxy and NGC 891 is almost entirely a disk galaxy. Fraternali *et al.* [60] asks "why are these RCs so identical if their dark matter halos are necessarily different to accommodate the differences in the luminous mass?"

In the RCFM paradigm the two RCs are very similar in magnitude, but differ markedly in their inflections at large radii. In the RCFM paradigm, the inflection indicates the relative galaxy baryon mass with respect to the Milky Way. NGC 7814 inflects up, whereas NGC 891 inflects down. RCFM fits to these galaxies are successful, see Fig.9 and Tables III and, IV. We report here fits to the Fraternali *et al.* [60] RC, which is included in the SPARC database.

TABLE III: **Results for bulge dominated NGC 7814**

Model	γ_d	γ_b	χ^2
Dark Matter Iso	0.68	0.71	0.39
MOND-RAR	1.17	0.52	1.334
RCFM	0.41	0.67	1.20

(a) The NGC 7814 RC data from [60], and resulting γ_i are in units of solar mass per solar luminosity $M_\odot/L_\odot$.

TABLE IV: **Results for disk dominated NGC 891 from [60] RC data.**

Model	γ_d	γ_b	χ^2
Dark Matter Iso	0.77	1.63	1.30
MOND-RAR	0.32	—	25.16
RCFM	0.66	0.03	1.56

5. NGC 5055

The SPARC database for NGC 5055 uses HI RC data from [61], and a luminous model with no bulge. They a report their model and RC data at at a reliable distance of 9.83 ± 0.30 Mpc, from the Tip of The Red Giant Branch method.

TABLE V: **Results for NGC 5055 in SPARC from [61] RC data.**

Model	γ_d	γ_b	χ^2
MOND-RAR	0.56	-	7.42
RCFM	0.62	-	6.03

To compare NGC 5055 RCFM fits to both MOND and dark matter models, we include here RC data from THINGS [56] in Fig.12, at a reported distance of $10.1 \pm .0$ Mpc from the Hubble Flow and with a stellar bulge included in the mass modeling.

This galaxy serves as an example of the underconstrained nature of galaxy mass modeling [25] because both theories of dark matter and MOND invoke new physics. RCFM fits are as good as either competing mode, without modifying physics.

TABLE VI: **Results for bulge dominated NGC 5055 from [60] RC data.**

Model	γ_d	γ_b	χ^2
Dark Matter Iso	0.79	0.11	8.13
Dark Matter NFW	0.79	0.11	10.31
MOND-RAR	0.43	0.46	2.63
RCFM	0.57	0.23	1.30

E. Constraining the RCFM Free Parameter

We test a functional form for the model's free parameter α, based on photometric quantities. We select a subset of galaxies with the most reliable distances and RC data [17] by the following criteria:

1. photometry interpreted with most reliable distance methods (tip of the red giant branch, and Cepheid variable stars, with errors in distance on the order of $5\% - 10\%$), rejecting all other galaxies.

2. inclination angle on the sky in the range $[15^o, 80^o]$, rejecting galaxies with an inclination greater than 80^o as impossible to constrain the surface brightness profile, and those at inclinations less than 15^o as being impossible to report line of sight Doppler shifts accurately.

3. Lelli *et al.* [17] report a quality factor for each galaxy in the SPARC database, assigning $Q = 3$ to galaxies not suited to dynamical studies due to asymmetries, non-circular motions, and/or offsets between stars and gas. Galaxies with Q = 3 are rejected from our subset.

By this process, we select a subset of 36 galaxies as reported in Table VIII.

We then plot the α parameter space versus the ratio of photometric quantities,

$$L_{total}/R_{eff}, \tag{18}$$

for L_{total} the total luminosity of the galaxy as measured at a wavelength of $3.6\mu m$, assuming a solar absolute magnitude of 3.24 at $3.6\mu m$ [63] in units of 10^9 solar $L_\odot$, and the effective radius R_{eff} the length encompassing half of the total luminosity [17] in units of kiloparsecs. The resulting distribution (Fig. 13) is well fitted by the function

$$\alpha = 51.5(L_{total}/R_{eff})^{-1.03} \tag{19}$$

at an $R^2 = .81\%$.

V. CONCLUSIONS

At this time, there are many discrepancies between concordance cosmology theory and observations at different length scales and in different physical problems being resolved by dark matter models [64–66]. (Rich's note: I don't really like this sentence, we might want to edit it). In this paper we address only one, the flat-rotation curve problem of spiral galaxies. This choice is due to the very clear presentation possible. Other dark matter problems require cosmological model assumptions which are beyond the scope of the current problem.

We re-interpret the flat-rotation curve problem, at the level of the data, as a problem of excesses in Doppler shifted spectra due to relative frame effects from our home galaxy. We predict that the flat-rotation curve problem is an artifact of misinterpretation of Doppler shifted spectra from external galaxies, removing the need for dark matter halos on galaxies. This framing places primary importance on the role of the Milky Way, and compactly explains both why the Milky Way sits roughly at the inflection point in the Universal Rotation Curve spectrum of 1,100 galaxies [9] and why MOND is both successful and limited.

The rotation curve fitting model (RCFM) presented here reproduces the fitting successes of MOND and dark matter models on as sample of 175 well studied galaxy rotation curves[17], but does not modify classical physics. We emphasize that the only input to the RCFM is the luminous mass. Independent of the interpretation of the various quantities appearing in the formulae presented here, this is a one parameter fit to the data. What is more, the one free parameter appears to be highly correlated to the ratio of the observable photometric parameters luminosity and effective radius. This model is fasifiable and appears to be supported by the recent GAIA data release Jiao *et al.* [38], which indicates a Keplerian descent of the Milky Way rotation curve beyond our position at $\approx$ 8 kpc, from 10 - 26.5 kpc. The upcoming Large Survey of Space and Time at the Vera C. Rubin Observatory [67–70] will further constrain the Milky Way rotation curve past 26.5 kpc. (Sofia note to Rich & Meagan & Marcus, IDK know if these last two sentences are worded well.).

VI. ACKNOWLEDGMENTS

This work is dedicated to Emmett Till. We acknowledge and express gratitude to the first nations peoples on whose unceded lands this was written; including but not limited, to the Coast Salish bands of the Puget Sound, the Cheyenne, Arapaho and Southern Ute Peoples of Colorado, and the Algonquian and Iroquoian Peoples of Massachusetts and New York. The authors would like to thank V. P. Nair, T. Boyer, I. Chavel, R. Walterbos, S. McGaugh, and A. Klypin.

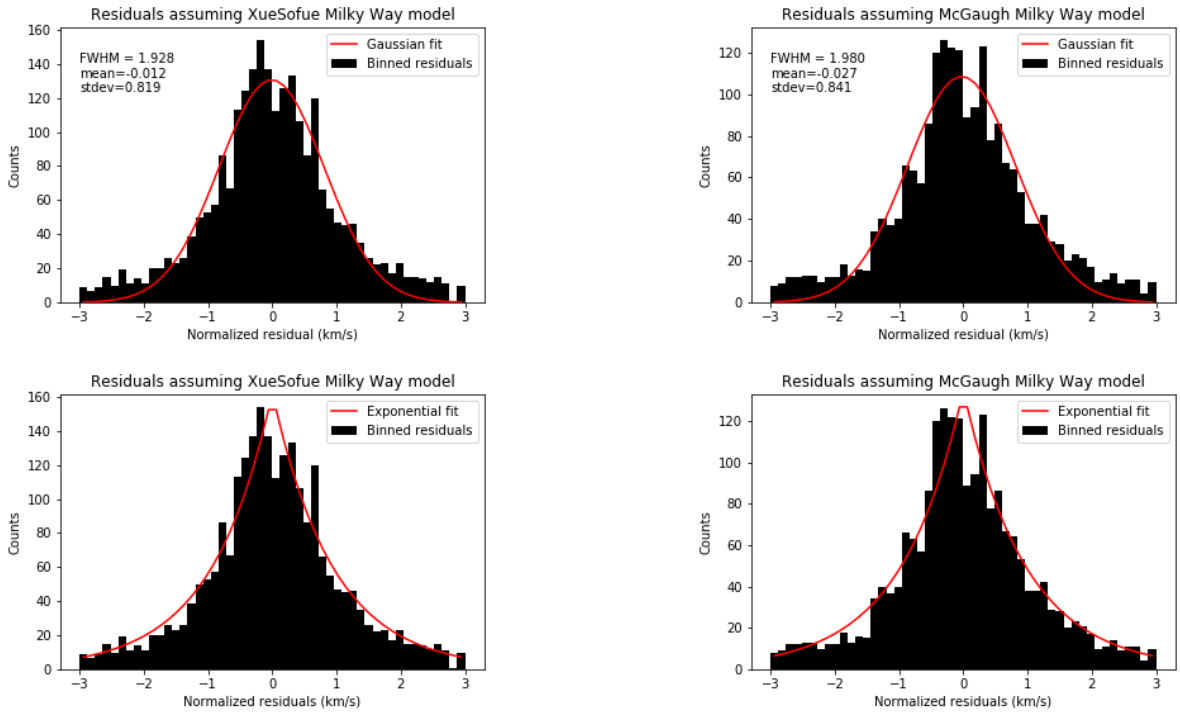

FIG. 3: Normalized residuals from fits assuming either Xue-Sofue of McGaugh Milky Way models, fitted to a Gaussian or exponential function. The full-width half-maximums, means, and standard deviations are shown for the Gaussian fits. The exponential fits capture peak and tails in residuals better than the Gaussian fits, suggesting non-Gaussian behavior in the error of velocity observations.

TABLE VII: **Training Set to determine the RCFM free parameter α functional form**

Galaxy Name	Hubble Type(1)	Distance (Mpc)	Mean Error on D (Mpc)	Distance Method (2)	Inc (deg)(3)
CamB	10	3.36	0.26	2	65
D564-8	10	8.79	0.28	2	63
D631-7	10	7.72	0.18	2	59
DDO154	10	4.04	0.2	2	64
DDO168	10	4.25	0.21	2	63
ESO444-G084	10	4.83	0.48	2	32
IC2574	9	3.91	0.2	2	75
NGC0024	5	7.3	0.36	2	64
NGC0055	9	2.11	0.11	2	77
NGC0247	7	3.7	0.19	2	74
NGC0300	7	2.08	0.1	2	42
NGC2403	6	3.16	0.16	2	63
NGC2683	3	9.81	0.49	2	80
NGC2841	3	14.1	1.4	3	76
NGC2915	11	4.06	0.2	2	56
NGC2976	5	3.58	0.18	2	61
NGC3109	9	1.33	0.07	2	70
NGC3198	5	13.8	1.4	3	73
NGC3741	10	3.21	0.17	2	70
NGC4068	10	4.37	0.22	2	44
NGC4214	10	2.87	0.14	2	15
NGC5055	4	9.9	0.3	2	55
NGC6503	6	6.26	0.31	2	74
NGC6789	11	3.52	0.18	2	43
NGC6946	6	5.52	1.66	2	38
NGC7331	3	14.7	1.5	3	75
NGC7793	7	3.61	0.18	2	47
UGC04483	10	3.34	0.31	2	58
UGC07232	10	2.83	0.17	2	59
UGC07524	9	4.74	0.24	2	46
UGC07559	10	4.97	0.25	2	61
UGC07577	10	2.59	0.13	2	63
UGC07866	10	4.57	0.23	2	44
UGC08490	9	4.65	0.53	2	50
UGC08837	10	7.21	0.36	2	80
UGCA442	9	4.35	0.22	2	64
UGCA444	10	0.98	0.05	2	78

TABLE VIII: (UPDATED TSet on Git Master 2.8.23). (1) Hubble type of: 0 = S0, 1 = Sa, 2 = Sab, 3 = Sb, 4 = Sbc, 5 = Sc, 6 = Scd, 7 = Sd, 8 = Sdm, 9 = Sm, 10 = Im, 11 = BCD. (2) Distance method: 2 = tip of the red giant branch, 3 = Cepheids. (3) Inclination on the sky. All table information from Lelli *et al.* [17].

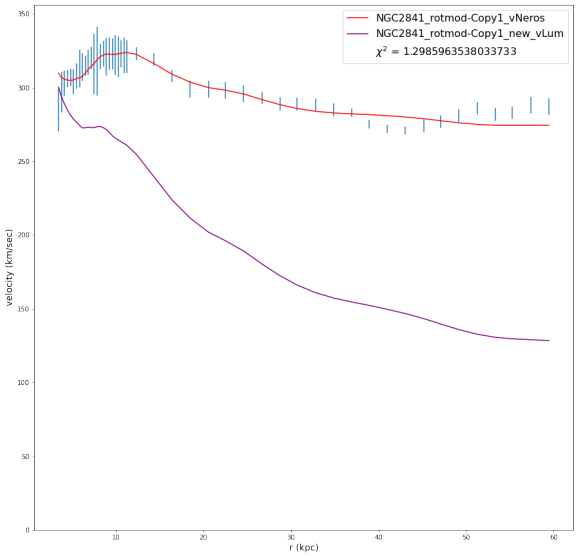

FIG. 4: RCFM fit (red line) to star dominated galaxy NGC2841. Purple line is the estimated Keplerian velocity due to luminous mass, and blue data points with error bars are the RC data traced by an orange line. Fitted at the Cepheid distance 14.1 Mpc, with resulting mass-to-light ratios of $\gamma_d = 0.87$ and $\gamma_b = 1.11$, and reduced $\chi^2_\nu = 1.30$.

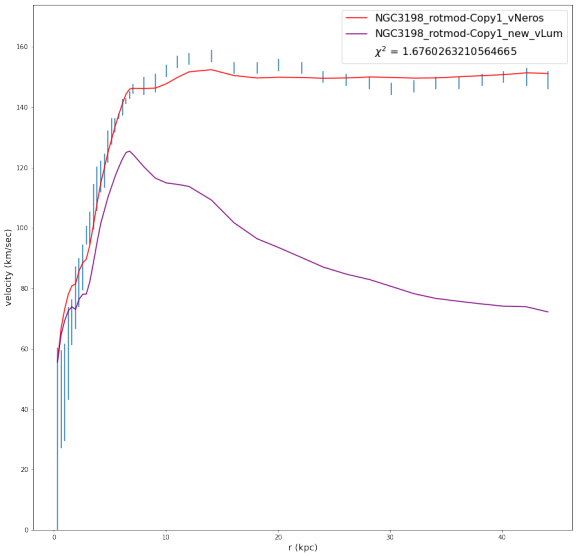

FIG. 6: RCFM Fit (red line) to NGC 3198, fitted at Cepheid distance 13.8Mpc, velocity estimated from luminous mass is the purple line, and orange line traces the RC data (blue points with error bars). RCFM results $\gamma_d = 0.878$, $\chi^2_\nu = 1.676$. RC data [17]

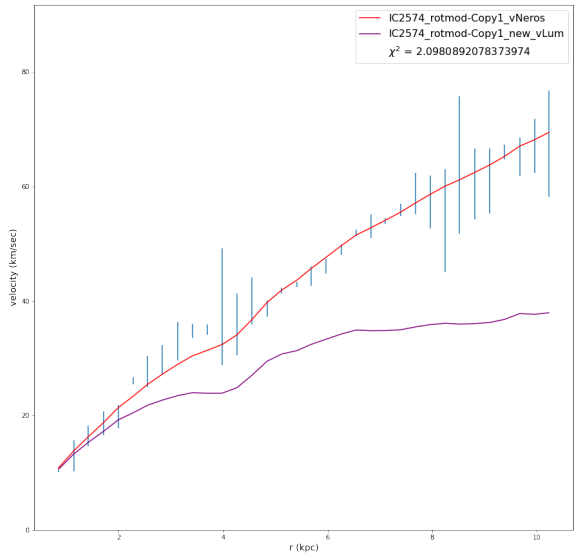

FIG. 5: RCFM fit to gas dominated IC 2574, at the reported distance 3.780.19 Mpc from tip of the red giant branch, $\gamma_d = 1.105$ (raw), and reduced $\chi^2_\nu = 2.098$.Lines are as in Fig. 4

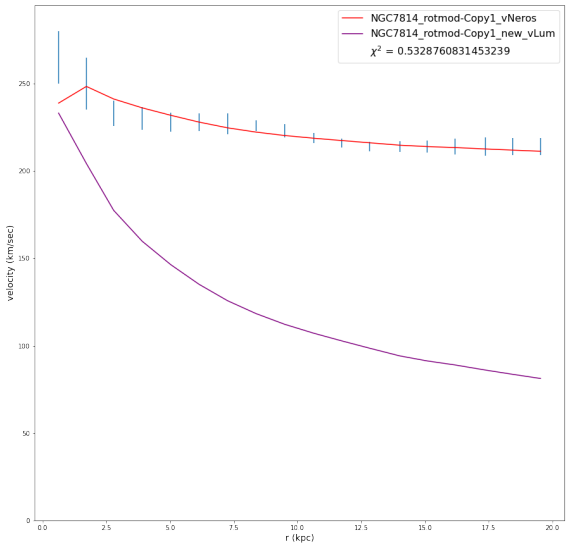

FIG. 7: RCFM fit to Bulge dominated NGC 7814, RC data from SPARC[17].

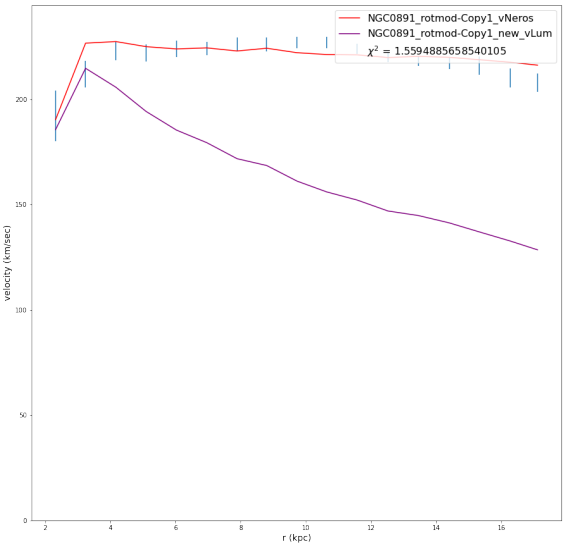

FIG. 8: RCFM fit to Disk dominated NGC 891, RC data from SPARC[17],

FIG. 9: Comparison of fits for NGC 7814 and NGC 891. Both edge-on galaxies with similar total light, but very different distributions of that light. RCFM fits (red line), points with error bars are the RC data, and the input baryonic mass models is the purple lines.

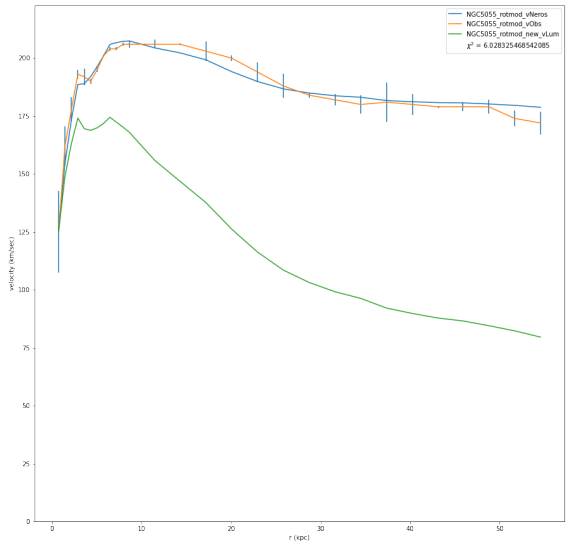

FIG. 10: RCFM fit to NGC 5055, RC data and luminous mass model from SPARC[17].

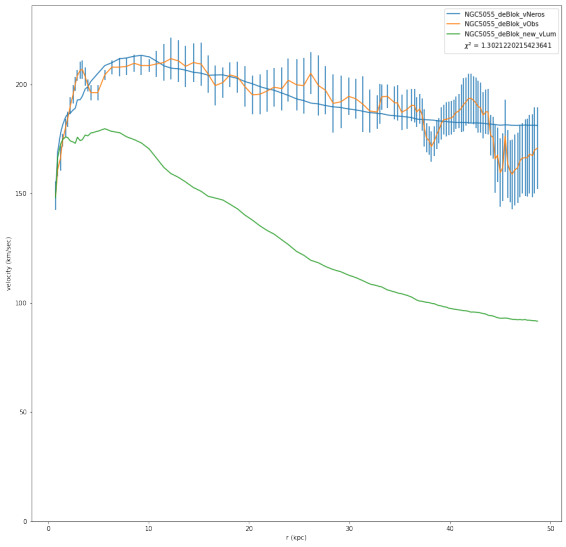

FIG. 11: RCFM fit to NGC 5055, RC data and luminous mass model from de Blok (THINGS)[62],

FIG. 12: Comparison of fits for NGC 5055 for different RC data and luminous mass models. RCFM fits are the blue lines, points with error bars traced by orange lines are the RC data, and the input baryonic mass models are the green lines.

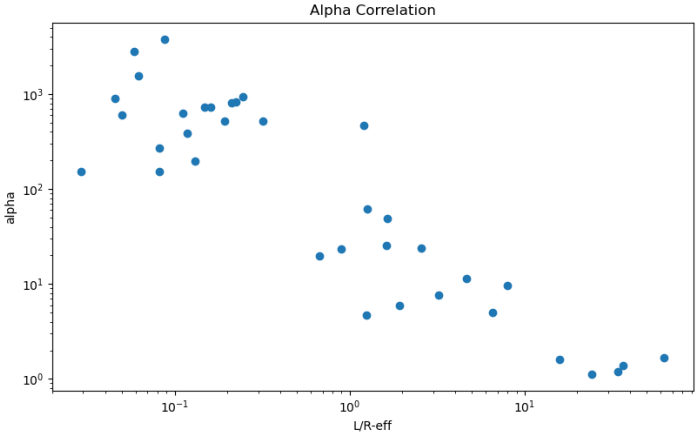

FIG. 13: Correlation of RCFM free parameter α with ratio of L total luminosity in units of 10^9 solar $L_\odot$, and R_{eff} is the effective or half-light radius in kpc. This subset of the SPARC Galaxies has been selected by best distance estimates (Cepheids and Tip of the Red Giant Branch). For a full list of galaxies see Table VIII. REMAKE Daniel Lopez. Errors SPARC estimates of 20 for LUM.

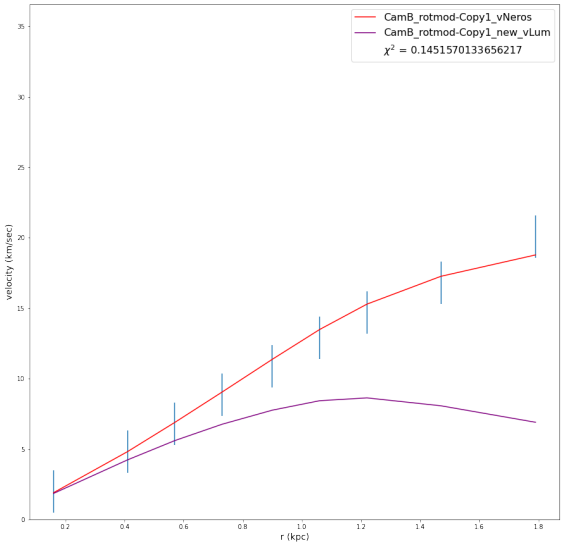

FIG. 14: CamB : SPARC[17]

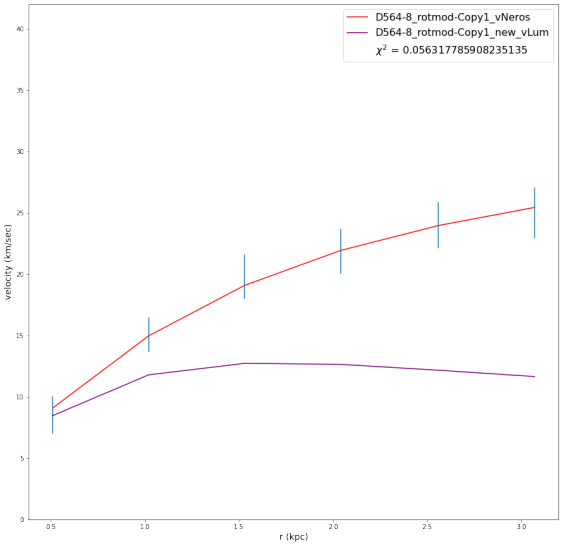

FIG. 15: D564-8 : SPARC[17]

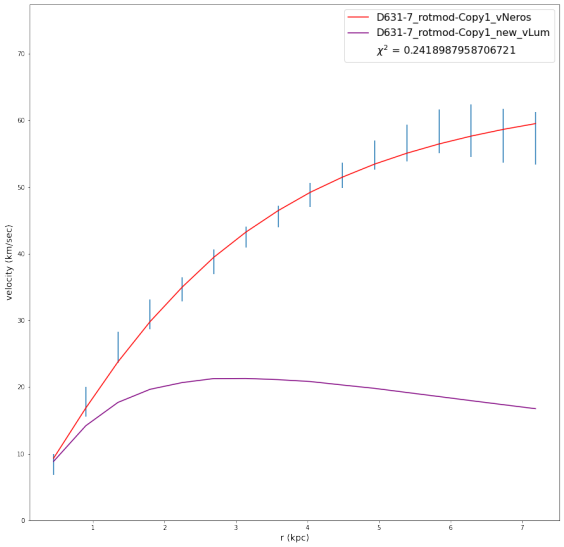

FIG. 16: D631-7 SPARC[17]

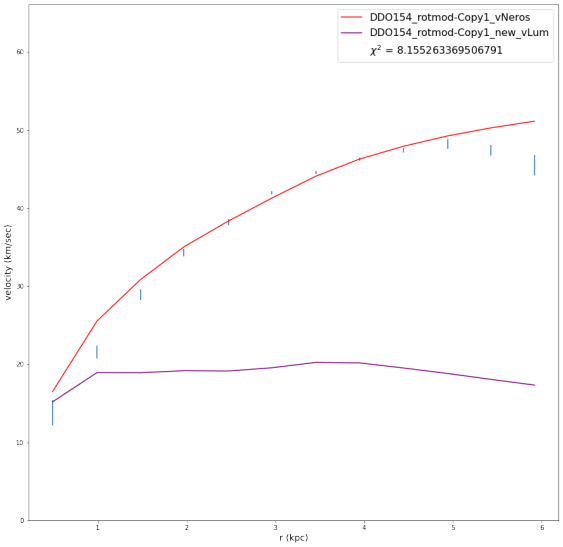

FIG. 17: DD00154 : SPARC[17]

FIG. 18: Examples of gas dominated, dwarf galaxies. RCFM rotation curve fits (red line), blue points with error bars are the rotation curve data, and the input baryonic mass model is the purple line.

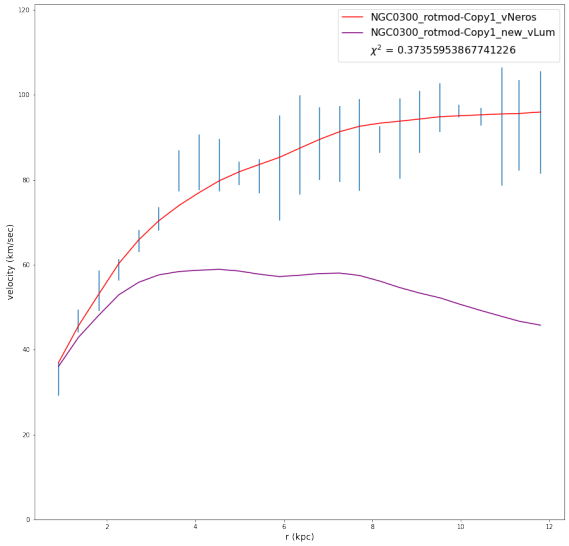

FIG. 19: NGC0300 SPARC[17]

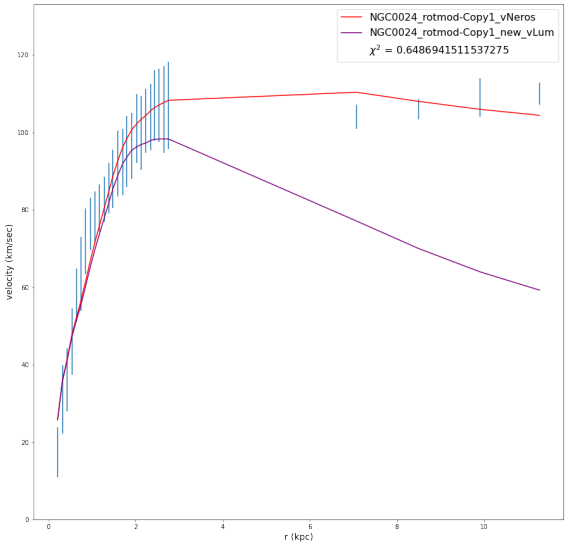

FIG. 20: NGC0024 SPARC[17]

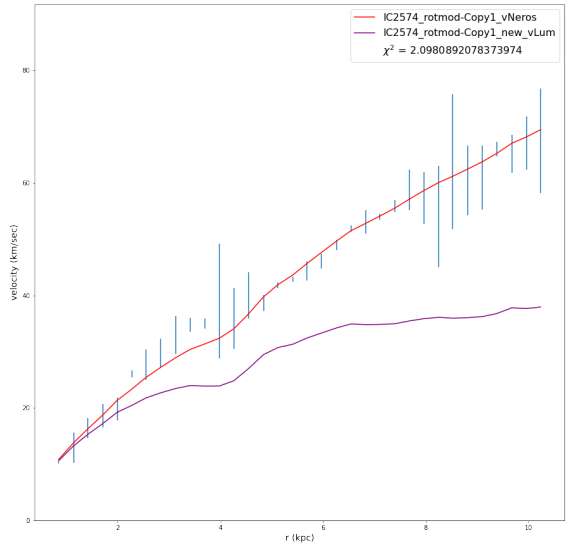

FIG. 21: IC2574 SPARC[17]

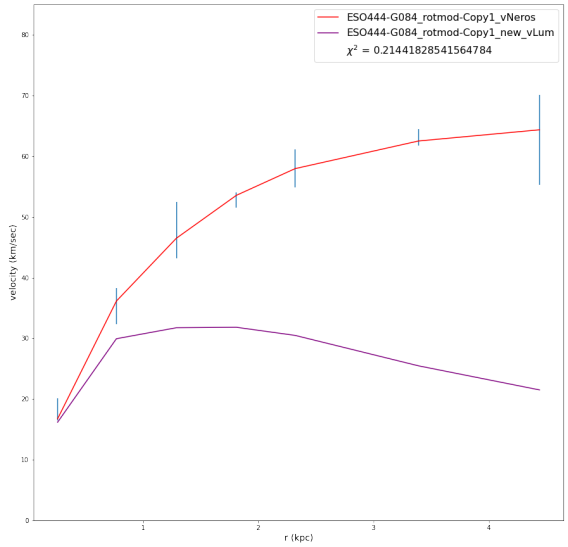

FIG. 22: ESO444-G084 SPARC[17]

FIG. 23: RCFM rotation curve fits (red line), blue points with error bars are the rotation curve data, and the input baryonic mass models are the purple lines.

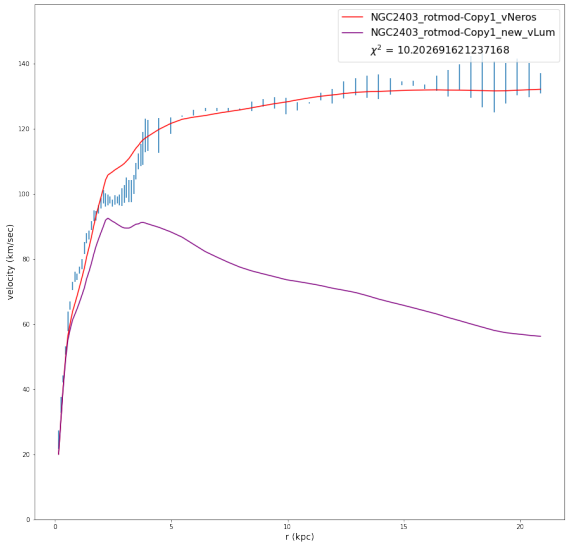

FIG. 24: NGC2403 SPARC[17]

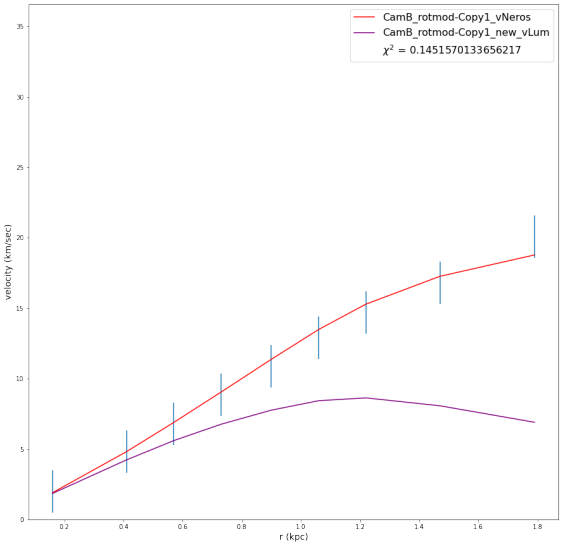

FIG. 25: CamB from SPARC[17]

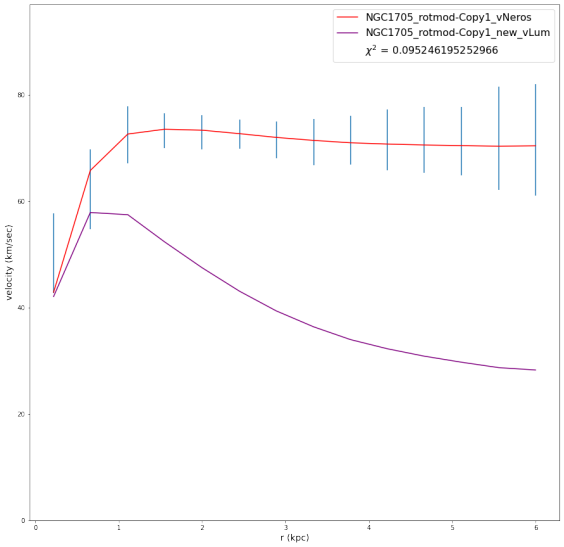

FIG. 26: NGC1705 SPARC[17]

FIG. 27: RCFM rotation curve fits (red line), blue points with error bars are the rotation curve data, and the input baryonic mass models are the purple lines.

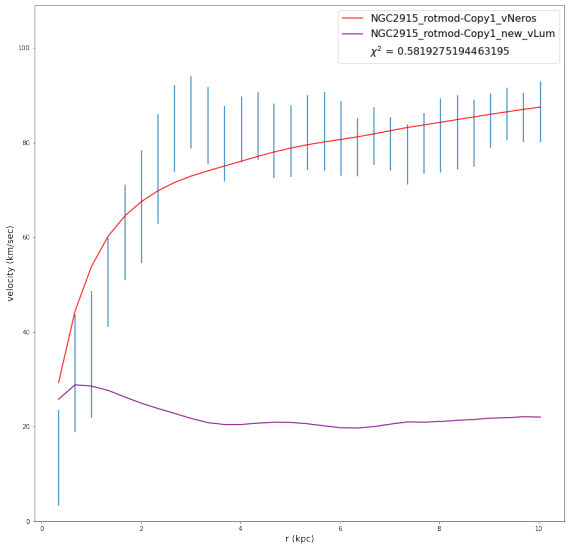

FIG. 28: NGC 2915 SPARC[17]

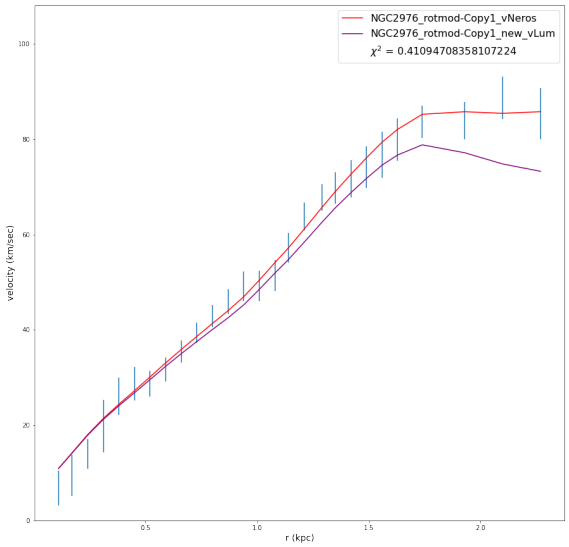

FIG. 29: NGC 2976

FIG. 30: RCFM rotation curve fits (red line), blue points with error bars are the rotation curve data, and the input baryonic mass models are the purple lines.

TABLE IX: **UNDER CONSTRUCTION Comparison of Fit Results from MOND-RAR and RCFM**

Galaxy name	**log (L[3.6])**	**RAR**	**RAR**	**RAR**	**RCFM**	**RCFM**	**RCFM**
	units ($L_\odot$)	γ_{disk}	γ_{bulge}	χ^2	χ^2	γ_{disk}	γ_{bulge}
CamB	7.88	0.34	...	5.758	0.145	1.43E-05	...
D512-2	8.51	0.48	...	0.37	0.052	1.48	...
D564-8	7.52	0.40	...	3.16	0.056	1.22	...
D631-7	8.29	0.20	...	15.872	0.242	0.28	...
DDO064	8.2	0.48	...	0.334	0.357	1.58	...
DDO154	7.72	0.19	...	3.482	8.155	1.20	...
DDO161	8.74	0.23	...	1.468	0.585	0.98	...
DDO168	8.28	0.46	...	19.714	3.087	0.79	...
DDO170	8.73	0.79	...	4.917	2.006	1.84	...
ESO079-G014	10.71	0.50	...	4.334	3.081	1.09	...
ESO116-G012	9.63	0.35	...	2.444	0.842	1.04	...
ESO444-G084	7.85	0.42	...	3.253	0.214	1.87	...
ESO563-G021	11.49	0.43	...	28.836	14.570	0.99	...
F561-1	9.61	0.52	...	—	—	—	...
F563-1	9.28	0.56	...	1.499	0.788	2.07	...
F563-V1	9.19	0.48	...	0.875	0.143	0.99	...
F563-V2	9.48	0.59	...	0.991	0.079	2.20	...
F565-V2	8.75	0.50	...	0.474	0.181	2.23	...
F567-2	9.33	0.56	...	2.204	0.200	1.31	...
F568-1	9.8	0.61	...	1.287	0.539	1.91	...
F568-3	9.92	0.41	...	3.064	1.500	1.31	...
F568-V1	9.58	0.81	...	1.042	0.109	2.14	...
F571-8	10.01	0.11	...	41.61	1.550	0.18	...
F571-V1	9.27	0.50	...	0.288	0.116	1.49	...
F574-1	9.82	0.71	...	2.501	1.125	1.54	...
F574-2	9.46	0.49	...	0.092	0.0559	0.67	...
F579-V1	10.07	0.63	...	2.559	0.844	1.63	...
F583-1	8.99	0.91	...	2.663	0.926	1.87	...
F583-4	9.23	0.48	...	0.134	0.208	1.30	...
IC2574	9.01	0.07	...	1.44	2.098	1.11	...
IC4202	11.25	1.60	0.34	41.908	11.571	6.28E-06	0.449
KK98-251	7.93	0.44	...	1.227	0.336	1.67	...
NGC0024	9.59	1.01	...	0.85	0.649	1.39	...
NGC0055	9.67	0.19	...	1.579	2.508	1.02	...
NGC0100	9.51	0.28	...	1.286	0.089	0.93	...
NGC0247	9.87	0.78	...	3.06	1.925	1.53	...
NGC0289	10.86	0.92	...	2.132	1.563	0.74	...
NGC0300	9.47	0.40	...	0.906	0.374	1.14	...
NGC0801	11.49	1.33	...	7.753	5.886	0.76	...
NGC0891	11.14	0.33	0.40	7.368	2.983	0.42	0.749
NGC1003	9.83	0.37	...	4.669	2.951	0.78	...
NGC1090	10.86	0.74	...	2.778	1.985	0.81	...
NGC1705	8.73	1.22	...	0.373	0.095	1.25	...
NGC2366	8.37	0.24	...	1.934	2.108	1.06	...
NGC2403	10	0.51	...	14.142	10.203	0.86	...
NGC2683	10.91	0.55	0.73	3.37	0.737	0.88	0.424
NGC2841	11.27	0.81	0.93	1.515	1.299	0.87	1.105
NGC2903	10.91	0.21	...	20.637	6.904	0.62	...
NGC2915	8.81	0.32	...	4.017	0.582	0.57	...
NGC2955	11.5	0.37	0.84	3.906	4.058	0.38	0.873
NGC2976	9.53	0.35	...	1.73	0.411	0.91	...
NGC2998	11.18	0.82	...	2.94	2.918	0.87	...
NGC3109	8.29	0.21	...	4.133	0.245	2.05	...
NGC3198	10.58	0.77	...	2.057	1.676	0.88	...
NGC3521	10.93	0.46	...	0.51	0.732	0.70	...

Cont'd on following page

TABLE IX, cont'd.

Galaxy name	**log (L[3.6]) units ($L_\odot$)**	**MOND—RAR** γ_{disk}	**MOND—RAR** γ_{bulge}	**MOND—RAR** χ^2	**RCFM** χ^2	**RCFM** γ_{disk}	**RCFM** γ_{bulge}
NGC3726	10.85	0.47	...	2.982	1.798	0.76	...
NGC3741	7.45	0.31	...	0.767	0.546	0.72	...
NGC3769	10.27	0.41	...	0.949	0.568	0.71	...
NGC3877	10.86	0.40	...	10.221	6.979	0.87	...
NGC3893	10.77	0.45	...	0.997	0.402	0.73	...
NGC3917	10.34	0.55	...	4.603	2.218	1.14	...
NGC3949	10.58	0.44	...	0.547	0.435	0.73	...
NGC3953	11.15	0.59	...	3.424	0.474	0.90	...
NGC3972	10.16	0.50	...	2.074	1.459	1.03	...
NGC3992	11.36	0.76	...	3.465	1.181	1.04	...
NGC4010	10.24	0.36	...	2.741	1.429	0.85	...
NGC4013	10.9	0.35	0.79	1.807	1.379	0.55	1.428
NGC4051	10.98	0.45	...	2.491	1.087	0.81	...
NGC4068	8.37	0.38	...	2.519	0.138	0.80	...
NGC4085	10.34	0.35	...	9.088	1.623	0.58	...
NGC4088	11.03	0.40	...	0.664	0.650	0.63	...
NGC4100	10.77	0.76	...	1.658	1.672	0.95	...
NGC4138	10.64	0.55	0.69	2.492	0.424	0.98	6.18E-05
NGC4157	11.02	0.43	0.64	0.72	0.489	0.69	0.563
NGC4183	10.03	0.79	...	1.132	0.457	1.25	...
NGC4214	9.06	0.46	...	1.062	0.925	1.02	...
NGC4217	10.93	1.17	0.17	3.171	1.118	1.13	0.455
NGC4389	10.33	0.30	...	9.313	0.104	0.31	...
NGC4559	10.29	0.52	...	0.496	0.318	0.77	...
NGC5005	11.25	0.54	0.56	0.091	0.065	0.59	0.685
NGC5033	11.04	1.03	0.43	8.024	5.535	0.84	0.516
NGC5055	11.18	0.56	...	7.415	6.028	0.62	...
NGC5371	11.53	3.30	...	10.156	10.587	0.77	...
NGC5585	9.47	0.22	...	6.817	5.503	0.75	...
NGC5907	11.24	1.08	...	7.73	6.768	0.93	...
NGC5985	11.32	0.63	3.32	6.974	5.165	0.95	2.133
NGC6015	10.51	1.12	...	10.873	12.088	0.99	...
NGC6195	11.59	0.32	0.85	2.258	2.709	0.37	0.805
NGC6503	10.11	0.45	...	2.979	1.418	0.75	...
NGC6674	11.33	0.95	1.30	10.638	2.969	0.67	1.808
NGC6789	8	0.60	...	5.904	0.143	1.41	...
NGC6946	10.82	0.64	0.71	1.525	1.682	0.64	0.574
NGC7331	11.4	0.32	0.60	1.289	0.962	0.51	1.201
NGC7793	9.85	0.55	...	1.013	0.701	0.89	...
NGC7814	10.87	1.17	0.52	1.334	0.533	0.42	0.674
PGC51017	8.19	0.44	...	4.567	1.156	0.80	...
UGC00128	10.08	2.49	...	6.254	5.326	1.65	...
UGC00191	9.3	1.10	...	3.842	1.628	1.38	...
UGC00634	9.48	0.49	...	2.425	1.561	1.57	...
UGC00731	8.51	2.39	...	6.415	0.062	3.79	...
UGC00891	8.57	0.32	...	25.16	0.613	1.35	...
UGC01230	9.88	0.72	...	2.951	0.588	1.72	...
UGC01281	8.55	0.39	...	0.244	0.299	1.43	...
UGC02023	9.12	0.49	...	1.147	0.022	0.72	...
UGC02259	9.24	1.14	...	7.221	2.896	1.82	...
UGC02455	9.56	0.33	...	6.549	0.560	0.28	...
UGC02487	11.69	1.83	0.91	4.482	3.036	1.16	0.912
UGC02885	11.61	0.45	0.97	0.858	1.958	0.44	0.962
UGC02916	11.09	1.57	0.73	11.652	10.632	1.43	0.704
UGC02953	11.41	0.61	0.62	5.661	fails	1	1
UGC03205	11.06	0.73	1.32	4.196	2.720	0.68	1.057

Cont'd on following page

TABLE IX, cont'd.

Galaxy name	**log (L[3.6]) units ($L_\odot$)**	**MOND—RAR** γ_{disk}	**MOND—RAR** γ_{bulge}	**MOND—RAR** χ^2	**RCFM** χ^2	**RCFM** γ_{disk}	**RCFM** γ_{bulge}
UGC03546	11.01	0.68	0.51	0.907	1.040	0.62	0.598
UGC03580	10.12	0.29	0.11	2.291	2.014	0.52	0.416
UGC04278	9.12	0.53	...	2.597	0.795	1.01	...
UGC04305	8.87	0.71	...	2.024	1.552	0.88	...
UGC04325	9.31	0.94	...	9.429	2.326	1.87	...
UGC04483	7.11	0.43	...	0.869	0.326	1.28	...
UGC04499	9.19	0.51	...	1.776	1.040	1.15	...
UGC05005	9.61	0.45	...	0.315	0.070c	1.04	...
UGC05253	11.23	0.63	0.69	4.747	5.519	0.51	0.707
UGC05414	9.05	0.41	...	1.299	0.096	1.06	...
UGC05716	8.77	1.41	...	5.664	2.914	1.53	...
UGC05721	8.73	0.62	...	1.824	0.760	1.11	...
UGC05750	9.52	0.48	...	1.352	0.340	1.57	...
UGC05764	7.93	3.83	...	16.177	6.650	3.71	...
UGC05829	8.75	0.60	...	0.454	0.051	1.85	...
UGC05918	8.37	0.54	...	0.936	0.129	2.31	...
UGC05986	9.67	0.31	...	3.997	1.367	1.16	...
UGC05999	9.53	0.48	...	5.693	1.454	1.27	...
UGC06399	9.36	0.53	...	0.52	0.150	1.43	...
UGC06446	8.99	1.04	...	0.996	0.144	1.70	...
UGC06614	11.09	0.51	0.50	1.164	0.885	0.70	0.587
UGC06628	9.57	0.52	...	0.851	0.324	0.83	...
UGC06667	9.15	1.00	...	5.357	1.609	3.77	...
UGC06786	10.87	0.27	0.34	1.389	0.666	0.52 9	0.667
UGC06787	10.99	0.45	0.28	20.814	23.663	0.72	0.563
UGC06818	9.2	0.29	...	5.387	0.768	0.54	...
UGC06917	9.83	0.54	...	1.315	0.803	1.12	...
UGC06923	9.46	0.42	...	1.624	0.443	0.80	...
UGC06930	9.95	0.63	...	1.233	0.383	...	
UGC06973	10.73	0.17	0.39	15.579	0.266	0.39	0.708
UGC06983	9.72	0.77	...	1.392	0.643	1.26	...
UGC07089	9.55	0.36	...	0.426	0.109	0.95	...
UGC07125	9.43	0.92	...	1.599	0.931	1.09	...
UGC07151	9.36	0.50	...	3.751	0.954	1.15	...
UGC07232	8.05	0.46	...	6.169	0.189	0.82	...
UGC07261	9.24	0.56	...	0.827	0.829	1.22	...
UGC07323	9.61	0.41	...	0.66	0.183	0.97	...
UGC07399	9.06	0.59	...	1.895	0.729	1.55	...
UGC07524	9.39	0.79	...	1.839	1.344	1.59	...
UGC07559	8.04	0.31	...	2.602	0.121	0.97	...
UGC07577	7.65	0.24	...	5.794	0.037	0.67	...
UGC07603	8.58	0.34	...	1.772	0.401	1.07	...
UGC07608	8.42	0.48	...	0.734	0.187	2.03	...
UGC07690	8.93	0.60	...	1.525	0.235	1.05	...
UGC07866	8.09	0.45	...	0.26	0.040	1.26	...
UGC08286	9.1	1.05	...	2.637	2.180	1.66	...
UGC08490	9.01	0.86	...	0.337	0.145	1.27	...
UGC08550	8.46	0.74	...	1.552	0.493	1.35	...
UGC08699	10.7	0.63	0.70	0.989	0.835	0.56	0.758
UGC08837	8.7	0.20	...	2.349	0.432	0.79	...
UGC09037	10.84	0.20	...	2.259	1.362	0.58	...
UGC09133	11.45	1.64	1.10	6.937	7.232	0.732	0.697
UGC09992	8.53	0.51	...	1.076	0.017	1.30	...
UGC10310	9.24	0.62	...	1.762	0.066	1.54	...
UGC11455	11.57	0.38	...	6.545	3.576	0.76	...
UGC11557	10.08	0.42	...	3.175	0.683	0.61	...

Cont'd on following page

TABLE IX, cont'd.

Galaxy name	**log (L[3.6]) units ($L_\odot$)**	**MOND—RAR** γ_{disk}	**MOND—RAR** γ_{bulge}	**MOND—RAR** χ^2	**RCFM** χ^2	**RCFM** γ_{disk}	**RCFM** γ_{bulge}
UGC11820	8.99	1.01	...	1.988	0.946	1.25	...
UGC11914	11.18	0.22	0.48	1.731	1.507	0.09	0.874
UGC12506	11.14	1.12	...	1.981	1.079	1.34	...
UGC12632	9.11	1.08	...	1.803	0.166	1.87	...
UGC12732	9.22	1.07	...	0.496	0.137	1.52	...
UGCA281	8.29	0.37	...	0.469	0.158	1.23	...
UGCA442	8.15	0.44	...	7.65	0.547	2.29	...
UGCA444	7.08	0.49	...	0.33	0.089	3.79	...

[1] V. Rubin, W. Ford, and N. Thonnard, ApJ **238**, 471 (1980).
[2] A. Bosma, AJ **86**, 1791 (1981).
[3] T. S. van Albada, J. N. Bahcall, K. Begeman, and R. Sancisi, Astrophys. J. **295**, 305 (1985).
[4] S. Cebrián, in *10th Symposium on Large TPCs for Low-Energy Rare Event Detection* (2022) arXiv:2205.06833 [physics.ins-det].
[5] S. McGaugh, Conference Proceedings **182** (1999).
[6] S. S. McGaugh, F. Lelli, and J. M. Schombert, Phys. Rev. Lett. **117**, 201101 (2016).
[7] S. S. McGaugh, Astrophys. J. **609**, 652 (2004), arXiv:astro-ph/0403610 [astro-ph].
[8] M. Persic, P. Salucci, and F. Stel, MNRAS **281**, 27 (1996), astro-ph/9506004.
[9] M. Persic, P. Salucci, , and F. Stel, MNRAS **281**, 27 (1996).
[10] V. C. Rubin, N. Thonnard, and W. K. Ford, Jr., ApJ **225**, L107 (1978).
[11] P. Salucci, A. Lapi, C. Tonini, G. Gentile, I. Yegorova, and U. Klein, Monthly Notices of the Royal Astronomical Society **378**, 41 (2007), https://academic.oup.com/mnras/article-pdf/378/1/41/3959881/mnras0378-0041.pdf.
[12] S. S. McGaugh, Studies in History and Philosophy of Science **88**, 220 (2021).
[13] T. Maschberger, I. A. Bonnell, C. J. Clarke, and E. Moraux, Monthly Notices of the Royal Astronomical Society **439**, 234 (2014), https://academic.oup.com/mnras/article-pdf/439/1/234/5571048/stt2403.pdf.
[14] W. de Blok, F. Walter, , and E. Brinks, AJ **136**, 2648 (2008).
[15] M. Milgrom, ApJ **270**, 371 (1983).
[16] S. McGaugh, Galaxies **2**, 601–622 (2014).
[17] F. Lelli, S. S. McGaugh, and J. M. Schombert, AJ **152**, 157 (2016), arXiv:1606.09251.
[18] J. D. Bekenstein, Phys. Rev. D **70**, 083509 (2004).
[19] F. I. COOPERSTOCK and S. TIEU, International Journal of Modern Physics A **22**, 2293 (2007), https://doi.org/10.1142/S0217751X0703666X.
[20] B. Famaey and S. S. McGaugh, Living Reviews in Relativity **15**, 10 (2012).
[21] C. W. Misner, K. S. Thorne, and J. A. Wheeler, *San Francisco: W.H. Freeman and Co., 1973* (1973).
[22] P. Li, F. Lelli, S. McGaugh, and J. Schombert, Astronomy I& Astrophysics **615**, A3 (2018).
[23] E. F. Bell and R. S. de Jong, ApJ **550**, 212 (2001), astro-ph/0011493.
[24] J. Schombert, S. McGaugh, and F. Lelli, Monthly Notices of the Royal Astronomical Society **483**, 1496 (2018), https://academic.oup.com/mnras/article-pdf/483/2/1496/27089556/sty3223.pdf.
[25] C. Conroy, J. Gunn, and M. White, ApJ **699**, 486 (2009).
[26] A. A. Dutton, S. Courteau, R. de Jong, and C. Carignan, The Astrophysical Journal **619**, 218 (2005).
[27] S. Casertano, **203**, 735 (1983).
[28] J. Jackson, *Classical Electrodynamics*, 3rd ed. (John Wiley & Sons, Inc., New Jersey, USA, 1999).
[29] S. Cisneros, G. Goedecke, C. Beetle, and M. Engelhardt, MNRAS **448**, 2733 (2015).
[30] M. Tecchiolli, Universe **5** (2019), 10.3390/universe5100206.
[31] E. Bertschinger, Ed Bertschinger Class NOTES.
[32] P. Jetzer, Physik-Institut der Universitat Zurich (2017).
[33] R. Wald, *General Relativity* (University of Chicago Press, Chicago, IL, USA, 1984).
[34] D. Pomarède, R. B. Tully, R. Graziani, H. M. Courtois, Y. Hoffman, and J. Lezmy, Astrophys. J. **897**, 133 (2020), arXiv:2007.04414 [astro-ph.CO].
[35] Y. Hoffman, D. Pomarede, R. Brent Tully, and H. Courtois, (2017), 10.1038/s41550-016-0036, arXiv:1702.02483 [astro-ph.CO].
[36] Y. B. Zel'dovich, Soviet Physics Uspekhi **11**, 381 (1968).
[37] W. Rindler, *Essential Relativity: Special, General, and Cosmological* (Springer New York, 2013).
[38] Y. Jiao, F. Hammer, H. Wang, J. Wang, P. Amram, L. Chemin, and Y. Yang, (2023), arXiv:2309.00048 [astro-ph.GA].
[39] T. H. Boyer, American Journal of Physics **79**, 644 (2011), arXiv:1008.1923 [physics.class-ph].
[40] S. Cisneros, N. Oblath, J. Formaggio, G. Goedecke, D. Chester, *et al.*, ARXIV:1309.7370 (2013), arXiv:1309.7370 [astro-ph.CO].
[41] S. Cisneros, N. Oblath, J. Formaggio, R. Ott, D. Chester, *et al.*, ARXIV:1407.7583 (2014), arXiv:1407.7583 [astro-ph.GA]CITATION = ARXIV:1407.7583 .
[42] S. Cisneros, J. G. O'Brien, N. S. Oblath, and J. A. Formaggio, ArXiv e-prints (2015), arXiv:1506.04587.
[43] S. Cisneros, J. O'Brien, N. Oblath, J. Formaggio, M. Crowley, and K. Mikulski, ArXiv e-prints (2016), arXiv:1608.08316.
[44] M. Schwarzschild, **59**, 273 (1954).
[45] K. C. Freeman, Astrophys. J. **160**, 811 (1970).
[46] T. Mistele, S. McGaugh, and S. Hossenfelder, **664**, A40 (2022), arXiv:2201.07282 [astro-ph.GA].

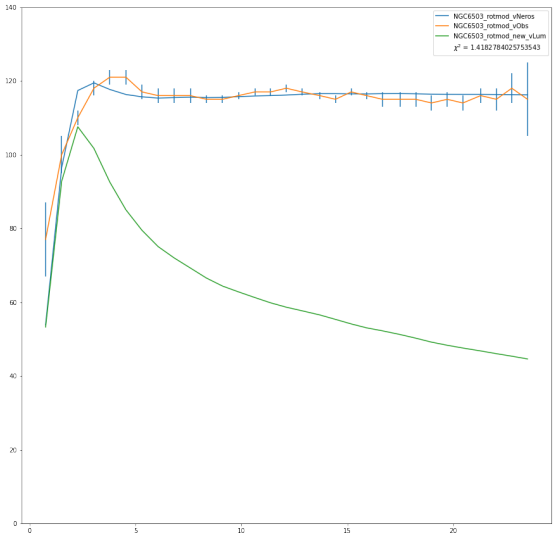

(a) Disk dominated NGC 6503

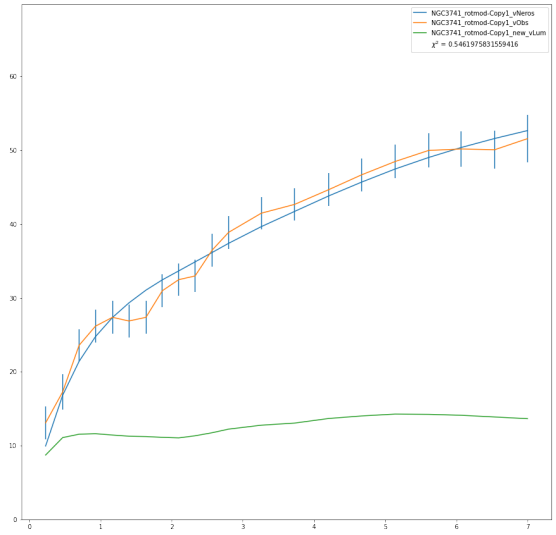

(b) Gas dominated NGC 3741

FIG. 31: Examples of range of spiral galaxy densities and RCFM rotation curve fits, orange lines trace the the rotation curve data which are the blue points with error bars, baryonic mass models are represented by the green lines, and the RCFM fit is the blue line. fit through data distracts from our fit)

[47] J. M. Huré and F. Hersant, **531**, A36 (2011), arXiv:1104.5079 [astro-ph.IM].
[48] T. Chatterjee, Ap&SS **139**, 243 (1987).
[49] M. Fich and S. Tremaine, **29**, 409 (1991).
[50] X. Xue *et al.* (SDSS Collaboration), AJ. **684**, 1143 (2008), arXiv:0801.1232 [astro-ph].
[51] Y. Sofue, "Mass Distribution and Rotation Curve in the Galaxy," in *Planets, Stars and Stellar Systems. Volume 5: Galactic Structure and Stellar Populations* (Oswalt, T. D. and Gilmore, G., 2013) p. 985.
[52] Y. Sofue, M. Honma, and T. Omodaka, Publications of the Astronomical Society of Japan **61**, 227 (2009).
[53] S. S. McGaugh, The Astrophysical Journal **885**, 87 (2019).
[54] J. F. Navarro, C. S. Frenk, and S. D. M. White, Astrophys. J. **462**, 563 (1996), arXiv:astro-ph/9508025 [astro-ph].
[55] A. Luna, L. Bronfman, L. Carrasco, and J. May, Astrophys. J. **641**, 938 (2006), arXiv:astro-ph/0512046 [astro-ph].
[56] W. de Blok, F. Walter, , and E. Brinks, AJ **136**, 2648 (2008).

[57] G. Gentile, B. Farnaey, and W. de Blok, A&A **527**, A76 (2011).
[58] F. Lelli, S. S. McGaugh, J. M. Schombert, and M. S. Pawlowski, The Astrophysical Journal **836**, 152 (2017).
[59] J. F. Navarro, A. Benítez-Llambay, A. Fattahi, C. S. Frenk, A. D. Ludlow, K. A. Oman, M. Schaller, and T. Theuns, **471**, 1841 (2017), arXiv:1612.06329 [astro-ph.GA].
[60] F. Fraternali, R. Sancisi, , and P. Kamphuis, A&A **http://arxiv.org/abs/1105.3867** (2011).
[61] G. Battaglia, F. Fraternali, T. Oosterloo, , and R. Sancisi, A& A **447**, 49 (2006).
[62] W. de Blok and S. McGaugh, MNRAS **290**, 533 (1997).
[63] S.-H. Oh, W. De Blok, F. Walter, E. Brinks, and R. C. Kennicutt, The Astronomical Journal **136**, 2761 (2008).
[64] R. H. Sanders, *The Dark Matter Problem: A Historical Perspective* (2010).
[65] R. B. Tully, H. Courtois, Y. Hoffman, and D. Pomarède, Nature **513**, 71 (2014), arXiv:1409.0880 [astro-ph.CO].
[66] R. P. Naidu, P. A. Oesch, P. van Dokkum, E. J. Nelson, K. A. Suess, G. Brammer, K. E. Whitaker, G. Illingworth, R. Bouwens, S. Tacchella, J. Matthee, N. Allen, R. Bezanson, C. Conroy, I. Labbe, J. Leja, E. Leonova, D. Magee, S. H. Price, D. J. Setton, V. Strait, M. Stefanon, S. Toft, J. R. Weaver, and A. Weibel, The Astrophysical Journal Letters **940**, L14 (2022).
[67] Željko Ivezić, S. M. Kahn, J. A. Tyson, B. Abel, E. Acosta, R. Allsman, D. Alonso, Y. AlSayyad, S. F. Anderson, J. Andrew, J. R. P. Angel, G. Z. Angeli, R. Ansari, P. Antilogus, C. Araujo, R. Armstrong, K. T. Arndt, P. Astier, Éric Aubourg, N. Auza, T. S. Axelrod, D. J. Bard, J. D. Barr, A. Barrau, J. G. Bartlett, A. E. Bauer, B. J. Bauman, S. Baumont, E. Bechtol, K. Bechtol, A. C. Becker, J. Becla, C. Beldica, S. Bellavia, F. B. Bianco, R. Biswas, G. Blanc, J. Blazek, R. D. Blandford, J. S. Bloom, J. Bogart, T. W. Bond, M. T. Booth, A. W. Borgland, K. Borne, J. F. Bosch, D. Boutigny, C. A. Brackett, A. Bradshaw, W. N. Brandt, M. E. Brown, J. S. Bullock, P. Burchat, D. L. Burke, G. Cagnoli, D. Calabrese, S. Callahan, A. L. Callen, J. L. Carlin, E. L. Carlson, S. Chandrasekharan, G. Charles-Emerson, S. Chesley, E. C. Cheu, H.-F. Chiang, J. Chiang, C. Chirino, D. Chow, D. R. Ciardi, C. F. Claver, J. Cohen-Tanugi, J. J. Cockrum, R. Coles, A. J. Connolly, K. H. Cook, A. Cooray, K. R. Covey, C. Cribbs, W. Cui, R. Cutri, P. N. Daly, S. F. Daniel, F. Daruich, G. Daubard, G. Daues, W. Dawson, F. Delgado, A. Dellapenna, R. de Peyster, M. de Val-Borro, S. W. Digel, P. Doherty, R. Dubois, G. P. Dubois-Felsmann, J. Durech, F. Economou, T. Eifler, M. Eracleous, B. L. Emmons, A. F. Neto, H. Ferguson, E. Figueroa, M. Fisher-Levine, W. Focke, M. D. Foss, J. Frank, M. D. Freemon, E. Gangler, E. Gawiser, J. C. Geary, P. Gee, M. Geha, C. J. B. Gessner, R. R. Gibson, D. K. Gilmore, T. Glanzman, W. Glick, T. Goldina, D. A. Goldstein, I. Goodenow, M. L. Graham, W. J. Gressler, P. Gris, L. P. Guy, A. Guyonnet, G. Haller, R. Harris, P. A. Hascall, J. Haupt, F. Hernandez, S. Herrmann, E. Hileman, J. Hoblitt, J. A. Hodgson, C. Hogan, J. D. Howard, D. Huang, M. E. Huffer, P. Ingraham, W. R. Innes, S. H. Jacoby, B. Jain, F. Jammes, M. J. Jee, T. Jenness, G. Jernigan, D. Jevremović, K. Johns, A. S. Johnson, M. W. G. Johnson, R. L. Jones, C. Juramy-Gilles, M. Jurić, J. S. Kalirai, N. J. Kallivayalil, B. Kalmbach, J. P. Kantor, P. Karst, M. M. Kasliwal, H. Kelly, R. Kessler, V. Kinnison, D. Kirkby, L. Knox, I. V. Kotov, V. L. Krabbendam, K. S. Krughoff, P. Kubánek, J. Kuczewski, S. Kulkarni, J. Ku, N. R. Kurita, C. S. Lage, R. Lambert, T. Lange, J. B. Langton, L. L. Guillou, D. Levine, M. Liang, K.-T. Lim, C. J. Lintott, K. E. Long, M. Lopez, P. J. Lotz, R. H. Lupton, N. B. Lust, L. A. MacArthur, A. Mahabal, R. Mandelbaum, T. W. Markiewicz, D. S. Marsh, P. J. Marshall, S. Marshall, M. May, R. McKercher, M. McQueen, J. Meyers, M. Migliore, M. Miller, D. J. Mills, C. Miraval, J. Moeyens, F. E. Moolekamp, D. G. Monet, M. Moniez, S. Monkewitz, C. Montgomery, C. B. Morrison, F. Mueller, G. P. Muller, F. M. Arancibia, D. R. Neill, S. P. Newbry, J.-Y. Nief, A. Nomerotski, M. Nordby, P. O'Connor, J. Oliver, S. S. Olivier, K. Olsen, W. O'Mullane, S. Ortiz, S. Osier, R. E. Owen, R. Pain, P. E. Palecek, J. K. Parejko, J. B. Parsons, N. M. Pease, J. M. Peterson, J. R. Peterson, D. L. Petravick, M. E. L. Petrick, C. E. Petry, F. Pierfederici, S. Pietrowicz, R. Pike, P. A. Pinto, R. Plante, S. Plate, J. P. Plutchak, P. A. Price, M. Prouza, V. Radeka, J. Rajagopal, A. P. Rasmussen, N. Regnault, K. A. Reil, D. J. Reiss, M. A. Reuter, S. T. Ridgway, V. J. Riot, S. Ritz, S. Robinson, W. Roby, A. Roodman, W. Rosing, C. Roucelle, M. R. Rumore, S. Russo, A. Saha, B. Sassolas, T. L. Schalk, P. Schellart, R. H. Schindler, S. Schmidt, D. P. Schneider, M. D. Schneider, W. Schoening, G. Schumacher, M. E. Schwamb, J. Sebag, B. Selvy, G. H. Sembroski, L. G. Seppala, A. Serio, E. Serrano, R. A. Shaw, I. Shipsey, J. Sick, N. Silvestri, C. T. Slater, J. A. Smith, R. C. Smith, S. Sobhani, C. Soldahl, L. Storrie-Lombardi, E. Stover, M. A. Strauss, R. A. Street, C. W. Stubbs, I. S. Sullivan, D. Sweeney, J. D. Swinbank, A. Szalay, P. Takacs, S. A. Tether, J. J. Thaler, J. G. Thayer, S. Thomas, A. J. Thornton, V. Thukral, J. Tice, D. E. Trilling, M. Turri, R. V. Berg, D. V. Berk, K. Vetter, F. Virieux, T. Vucina, W. Wahl, L. Walkowicz, B. Walsh, C. W. Walter, D. L. Wang, S.-Y. Wang, M. Warner, O. Wiecha, B. Willman, S. E. Winters, D. Wittman, S. C. Wolff, W. M. Wood-Vasey, X. Wu, B. Xin, P. Yoachim, and H. Zhan, The Astrophysical Journal **873**, 111 (2019).
[68] Abdurro'uf, K. Accetta, C. Aerts, V. Silva Aguirre, R. Ahumada, N. Ajgaonkar, N. Filiz Ak, S. Alam, C. Allende Prieto, A. Almeida, F. Anders, S. F. Anderson, B. H. Andrews, B. Anguiano, E. Aquino-Ortíz, A. Aragón-Salamanca, M. Argudo-Fernández, M. Ata, M. Aubert, V. Avila-Reese, C. Badenes, R. H. Barbá, K. Barger, J. K. Barrera-Ballesteros, R. L. Beaton, T. C. Beers, F. Belfiore, C. F. Bender, M. Bernardi, M. A. Bershady, F. Beutler, C. M. Bidin, J. C. Bird, D. Bizyaev, G. A. Blanc, M. R. Blanton, N. F. Boardman, A. S. Bolton, M. Boquien, J. Borissova, J. Bovy, W. N. Brandt, J. Brown, J. R. Brownstein, M. Brusa, J. Buchner, K. Bundy, J. N. Burchett, M. Bureau, A. Burgasser, T. K. Cabang, S. Campbell, M. Cappellari, J. K. Carlberg, F. C. Wanderley, R. Carrera, J. Cash, Y.-P. Chen, W.-H. Chen, B. Cherinka, C. Chiappini, P. D. Choi, S. D. Chojnowski, H. Chung, N. Clerc, R. E. Cohen, J. M. Comerford, J. Comparat, L. da Costa, K. Covey, J. D. Crane, I. Cruz-Gonzalez, C. Culhane, K. Cunha, Y. S. Dai, G. Damke, J. Darling, J. Davidson, James W., R. Davies, K. Dawson, N. De Lee, A. M. Diamond-Stanic, M. Cano-Díaz, H. D. Sánchez, J. Donor, C. Duckworth, T. Dwelly, D. J. Eisenstein, Y. P. Elsworth, E. Emsellem, M. Eracleous, S. Escoffier, X. Fan, E. Farr, S. Feng, J. G. Fernández-Trincado, D. Feuillet, A. Filipp, S. P. Fillingham, P. M. Frinchaboy, S. Fromenteau, L. Galbany, R. A. García, D. A. García-Hernández, J. Ge, D. Geisler, J. Gelfand, T. Géron, B. J. Gibson, J. Goddy, D. Godoy-Rivera, K. Grabowski, P. J. Green, M. Greener, C. J. Grier, E. Griffith, H. Guo, J. Guy, M. Hadjara, P. Harding, S. Hasselquist, C. R. Hayes, F. Hearty, J. Hernández, L. Hill, D. W. Hogg, J. A. Holtzman, D. Horta, B.-C. Hsieh, C.-H. Hsu, Y.-H. Hsu, D. Huber, M. Huertas-Company, B. Hutchinson, H. S. Hwang, H. J. Ibarra-Medel, J. I. Chitham, G. S. Ilha, J. Imig, W. Jaekle, T. Jayasinghe, X. Ji, J. A. Johnson, A. Jones, H. Jönsson, I. Katkov, D. Khalatyan, Arman, K. Kinemuchi, S. Kisku, J. H. Knapen, J.-P. Kneib, J. A. Kollmeier, M. Kong, M. Kounkel, K. Kreckel, D. Krishnarao, I. Lacerna, R. R. Lane, R. Langgin, R. Lavender, D. R. Law, D. Lazarz, H. W. Leung, H.-H. Leung, H. M. Lewis, C. Li, R. Li, J. Lian, F.-H. Liang, L. Lin, Y.-T. Lin, S. Lin, C. Lintott, D. Long, P. Longa-Peña, C. López-Cobá, S. Lu, B. F. Lundgren, Y. Luo, J. T. Mackereth, A. de la Macorra, S. Mahadevan, S. R. Majewski, A. Manchado, T. Mandeville, C. Maraston, B. Margalef-Bentabol, T. Masseron, K. L. Masters, S. Mathur, R. M. McDermid, M. Mckay, A. Merloni, M. Merrifield, S. Meszaros, A. Miglio, F. Di Mille, D. Minniti, R. Minsley, A. Monachesi, J. Moon, B. Mosser, J. Mulchaey, D. Muna, R. R. Muñoz, A. D. Myers, N. Myers, S. Nadathur, P. Nair, K. Nandra, J. Neumann, J. A. Newman, D. L. Nidever, F. Nikakhtar, C. Nitschelm, J. E. O'Connell, L. Garma-Oehmichen, G. Luan Souza de Oliveira, R. Olney, D. Oravetz, M. Ortigoza-Urdaneta, Y. Osorio, J. Otter, Z. J. Pace, N. Padilla, K. Pan, H.-A. Pan, T. Parikh, J. Parker, S. Peirani, K. Peña Ramírez, S. Penny, W. J. Percival, I. Perez-Fournon,

M. Pinsonneault, F. Poidevin, V. J. Poovelil, A. M. Price-Whelan, A. Bárbara de Andrade Queiroz, M. J. Raddick, A. Ray, S. B. Rembold, N. Riddle, R. A. Riffel, R. Riffel, H.-W. Rix, A. C. Robin, A. Rodríguez-Puebla, A. Roman-Lopes, C. Román-Zúñiga, B. Rose, A. J. Ross, G. Rossi, K. H. R. Rubin, M. Salvato, S. F. Sánchez, J. R. Sánchez-Gallego, R. Sanderson, F. A. Santana Rojas, E. Sarceno, R. Sarmiento, C. Sayres, E. Sazonova, A. L. Schaefer, R. Schiavon, D. J. Schlegel, D. P. Schneider, M. Schultheis, A. Schwope, A. Serenelli, J. Serna, Z. Shao, G. Shapiro, A. Sharma, Y. Shen, M. Shetrone, Y. Shu, J. D. Simon, M. F. Skrutskie, R. Smethurst, V. Smith, J. Sobeck, T. Spoo, D. Sprague, D. V. Stark, K. G. Stassun, M. Steinmetz, D. Stello, A. Stone-Martinez, T. Storchi-Bergmann, G. S. Stringfellow, A. Stutz, Y.-C. Su, M. Taghizadeh-Popp, M. S. Talbot, J. Tayar, E. Telles, J. Teske, A. Thakar, C. Theissen, A. Tkachenko, D. Thomas, R. Tojeiro, H. Hernandez Toledo, N. W. Troup, J. R. Trump, J. Trussler, J. Turner, S. Tuttle, E. Unda-Sanzana, J. A. Vázquez-Mata, M. Valentini, O. Valenzuela, J. Vargas-González, M. Vargas-Magaña, P. V. Alfaro, S. Villanova, F. Vincenzo, D. Wake, J. T. Warfield, J. D. Washington, B. A. Weaver, A.-M. Weijmans, D. H. Weinberg, A. Weiss, K. B. Westfall, V. Wild, M. C. Wilde, J. C. Wilson, R. F. Wilson, M. Wilson, J. Wolf, W. M. Wood-Vasey, R. Yan, O. Zamora, G. Zasowski, K. Zhang, C. Zhao, Z. Zheng, Z. Zheng, and K. Zhu, **259**, 35 (2022), arXiv:2112.02026 [astro-ph.GA].

[69] N. A. Bond, Ž. Ivezić, B. Sesar, M. Jurić, J. A. Munn, A. Kowalski, S. Loebman, R. Roškar, T. C. Beers, J. Dalcanton, C. M. Rockosi, B. Yanny, H. J. Newberg, C. Allende Prieto, R. Wilhelm, Y. S. Lee, T. Sivarani, S. R. Majewski, J. E. Norris, C. A. L. Bailer-Jones, P. Re Fiorentin, D. Schlegel, A. Uomoto, R. H. Lupton, G. R. Knapp, J. E. Gunn, K. R. Covey, J. Allyn Smith, G. Miknaitis, M. Doi, M. Tanaka, M. Fukugita, S. Kent, D. Finkbeiner, T. R. Quinn, S. Hawley, S. Anderson, F. Kiuchi, A. Chen, J. Bushong, H. Sohi, D. Haggard, A. Kimball, R. McGurk, J. Barentine, H. Brewington, M. Harvanek, S. Kleinman, J. Krzesinski, D. Long, A. Nitta, S. Snedden, B. Lee, J. R. Pier, H. Harris, J. Brinkmann, and D. P. Schneider, Astrophys. J. **716**, 1 (2010), arXiv:0909.0013 [astro-ph.GA].